This is a preprint, the final version is subject to change, of the American Mineralogist (MSA)
Cite as Authors (Year) Title. American Mineralogist, in press.
DOI: https://doi.org/10.2138/am-2019-6668

REVISION R1 version

Geochronology and trace element mobility in rutile from a Carboniferous syenite pegmatite and the role of halogens

GEORGIA PE-PIPER[1]*, JUSTIN NAGLE[1], DAVID J.W. PIPER[2] AND CHRIS R.M. MCFARLANE[3]

[1]Department of Geology, Saint Mary's University, Halifax, NS, B3H 3C3, Canada

[2]Natural Resources Canada, Geological Survey of Canada (Atlantic), Bedford Institute of Oceanography, P.O. Box 1006, Dartmouth, NS, B2Y 4A2, Canada

[3]Department of Earth Sciences, University of New Brunswick, 2 Bailey Drive, Fredericton, NB E3B 5A3, Canada

running head: Halogens and trace element mobility in rutile

*E-mail: gpiper@smu.ca +1 902 420 5744

ORCID G. Pe-Piper 0000-0002-7670-7358

ORCID D.J.W. Piper 0000-0002-6276-7560

This is a preprint, the final version is subject to change, of the American Mineralogist (MSA)
Cite as Authors (Year) Title. American Mineralogist, in press.
DOI: https://doi.org/10.2138/am-2019-6668

ABSTRACT

This study investigates Ti mobility in the presence of halogens, as shown by the hydrothermal alteration of magmatic rutile in syenite. The syenite pegmatite studied intrudes gabbro, is preserved as a tectonic block in major strike-slip fault zone, and formed in a back-arc environment in which there was widespread A-type granite plutonism. Rutile was studied by SEM and Raman spectroscopy, trace elements were analyzed by LA-ICPMS, and age was determined by in-situ U-Pb analysis. Magmatic rutile in the syenite forms millimetric-scale crystals rimmed by magmatic titanite and magnetite and also occurs as smaller interstitial crystals. Hydrothermal alteration occurred preferentially along crystal margins and fractures by a layer-by-layer dissolution-reprecipitation process resulting in high Zr contents (~5000 ppm) in the rutile, together with enrichment in U and depletion in high field strength elements. The magmatic emplacement age of the syenite was ~ 360 Ma (dated rutile G) and no younger than 353.9 ± 5.7 Ma (mean Concordia age of interstitial rutile). The syenite was synchronous with the later phases of regional A-type granite plutonism. Most magmatic rutile has REE patterns either (a) with 1–50 times chondrite enrichment, LREE>HREE and a Eu anomaly, resulting from felsic melt inclusions, or (b) rather flat patterns with 0.1–10 times chondrite enrichment, present in ilmenite exsolution lamellae or inclusions. Later hydrothermal halogen-rich fluids, derived from dissolution of halite, produced widespread metasomatic scapolite in the syenite. These fluids also leached Ti and other HFSE, together with REE, from large fractured rutile crystals. Such fluids resulted in local dissolution-reprecipitation of Ti and Zr and resetting of the U-Pb system in the altered rutile, at 337.4±3.5 Ma. Normalized REE abundances in the hydrothermal rutile

45 show a U-shaped pattern, with greatest depletion in the MREE**.** Variations in dissolution
46 and transport of Zr and Ti by halogen-rich fluids affect the Zr in rutile geothermometer,
47 which yields unrealistic temperatures when applied in this study. More generally, the
48 complexities of rutile chemistry in this hydrothermal setting could be reproduced in
49 deeper subduction settings as a result of variations in halogen content of fluids released
50 by prograde metamorphism.

51 **Keywords**: rutile; halogens; zirconium; hydrothermal, dissolution-reprecipitation

52 ## INTRODUCTION

53 Rutile is the most common, naturally occurring, polymorph of TiO_2. It is a widely
54 distributed accessory mineral in igneous and metamorphic rocks and in mantle xenoliths.
55 It contains the minor elements Fe, Cr, and V, and is a major host for Nb, Ta, and other
56 high field strength elements (HFSE). In amphibolites and eclogites, it can be the major
57 repository of HFSE (Zack et al. 2002; Meinhold 2010) and it is generally accepted as
58 playing a role in HFSE depletion of arc magmas (Ryerson and Watson 1987).
59 Experimental data suggest that rutile favors incorporation of HFSE in the order Ta> Nb>
60 Hf> Zr (Foley et al. 2000, 2002; Klemme et al. 2005).
61 Rutile is generally thought to be chemically inert with respect to aqueous fluids
62 evolved during prograde metamorphism, and experimental data suggest that the solubility
63 of rutile in pure water is very low (Tropper and Manning 2005; Audetat and Keppler
64 2005). However, there is a growing body of evidence from natural systems (e.g. John et
65 al. 2011; Spandler et al. 2011), and experimental studies (e.g. Rapp et al. 2010; Hayden
66 and Manning 2011; Tanis et al. 2015) that rutile is increasingly more soluble in halogen-

bearing (e.g. F, Cl) aqueous fluids evolved during prograde metamorphism in subduction environments. Slab-derived fluids are not pure water, but rather contain significant amounts of dissolved alkalis (Na, K), halogens (F, Cl), and aluminosilicates (Si, Al) (Manning 2004).

This study investigates rutile hosted by a scapolite-rich syenite pegmatite (Owen and Greenough 1999) preserved as a megablock in a large scale fault breccia that outcrops in cliffs and foreshore at Clarke Head, Nova Scotia (Donohoe and Wallace 1985, p. 50–53) (Fig. 1b). The fault breccia is part of the core zone of the Carboniferous Minas Fault Zone (MFZ: Murphy et al. 2011) that separates the Avalon and Meguma terranes of the Appalachians (Fig. 1a). Other megablocks consist principally of Lower Carboniferous sedimentary rocks (Donohoe and Wallace, 1985), but also include a Late Devonian gabbro-granulite (Gibbons and Murphy 1995; Gibbons et al. 1996), diorite in igneous contact with likely Horton Group sandstones, and a gabbro body that hosts the syenite (Fig. 2A). All the blocks of igneous rocks appear geochemically related to the 370–354 Ma A–type granites and lesser Ti-rich gabbros of the Cobequid Highlands (Fig. 1; Pe-Piper and Piper 2003), which evolved in an extensional backarc setting (Papoutsa et al. 2016). The plutons show complex hydrothermal mineralization including sodic alteration by magmatic fluids and remobilization of REE that appears related to their back-arc position (Pe-Piper et al. 2017b). Some of this alteration has taken place through coupled dissolution-reprecipitation processes with distinctive textural signatures (Ruiz-Agudo et al., 2014; Altree-Williams et al., 2015).

The present study is focused on the rutile in the syenite and its purpose includes: 1) to establish the petrogenetic relationships of different types of rutile; 2) to date

different types of rutile; and 3) to establish how and why different types of rutile differ geochemically and to relate this to high level crustal behavior of rutile in the presence of back-arc magmatic fluids.

GEOLOGICAL AND PETROLOGICAL BACKGROUND

Tectonic setting

The western Cobequid Highlands (Fig. 1) to the north of Clarke Head are underlain by Neoproterozoic rocks of the Avalon terrane and late Devonian–early Carboniferous plutons and their extrusive equivalents, the Fountain Lake Group (Pe-Piper and Piper, 2003). The plutons consist principally of A-type granite, with lesser gabbro that typically has 2 wt% TiO_2 at Mg#=0.6 rising to 4 wt% at Mg#=0.3. To the south of the Cobequid Highlands is the Kennetcook basin, bounded to the north by the Kirkhill and Rockland Brook faults (Fig. 1a), with a fill of Early Carboniferous terrigenous clastic rocks (Horton Group) and overlying anhydrite, halite, limestone and red shales (Windsor Group).

Within the Cobequid Highlands, the Cobequid Shear Zone (CSZ) consists of a series of faults that were active during latest Devonian to earliest Carboniferous, including the faults bounding the Kennetcook basin. The dextral CSZ was part of the fault system marking the southeastern margin of the extensional Magdalen Basin, beneath the present Gulf of St Lawrence (Hibbard and Waldron, 2009). The Cobequid Highlands were in a back-arc setting with respect to Devonian subduction of the Rheic Ocean (Clarke et al., 1997).

In the middle Carboniferous, the CSZ was reactivated when the E–W-trending dextral Minas Fault Zone (MFZ) developed at the onset of the Alleghenian tectonic phase. Brittle deformation along the Cobequid Fault resulted in a highly cataclastic and blocky fault zone (MacInnes and White, 2004). The only other fault segment in the Cobequid Highlands with large-scale brecciation at this time is at Clarke Head.

Field observations at Clarke Head

Fault bounded, mega-breccia blocks at Clarke Head include foliated gabbro, undeformed gabbro, and diorite. At the large stack west of Clarke Head (Fig. 1b), gabbro with epidote veining was intruded by a coarse-grained syenite in the form of a stock and veins. Xenoliths of the gabbro are common in the syenite, at a range of scales, and some appear partly digested (Fig. 2A). They are not cognate enclaves as they lack chilled rims. In places, a hybrid monzonite is found at the gabbro-syenite contact (Fig. 2A). Hand specimen examination shows large crystals of K-feldspar, rutile, titanite, scapolite and analcime (Fig. 2B). Parts of the syenite are coarser (crystals up to 1 cm) and contain vugs, probably created by the escape of volatiles during the emplacement of the stock. These parts are referred to as pegmatitic, and include coarse-grained dark rutile crystals up to several mm in length (Fig. 3).

General petrology of syenite

The magmatic minerals identified in the syenite include K-feldspar as either perthite or untwinned crystals (Figs. 3, 4). Quartz is generally rare, but is locally common (e.g. Fig. 3A) and is largely hydrothermal. Other magmatic minerals include analcime I (late magmatic) and albite, generally interstitial but locally with larger crystals with interlocking texture (Fig. 4A). Rutile occurs as large prismatic crystals rimmed by titanite

I and titanomagnetite, both apparently magmatic (Figs. 3, 5A),and as smaller interstitial minerals (Fig. 3B, 5D). K-feldspar crystals have been largely replaced by scapolite and analcime II that now make up most of the rock (Figs. 3, 4 B, D), with analcime II probably replacing the albite in perthite. The large rutile-titanite-magnetite crystals together with K-feldspar that has largely altered to scapolite and analcime make up the framework of the rock

Veins and alteration in the syenite

The syenite appears vuggy in hand specimen and some vugs may be primary. In addition, secondary voids have been created by dissolution of primary rutile-titanite prismatic crystals. The syenite is cut by irregular veins and patches that are made up of chlorite + quartz ± calcite ± analcime III ± zircon together with voids (Figs. 3A, B, 5E,G). Such veins nowhere contain scapolite, although the timing of original fracturing is not constrained. Some titanite crystals in such veins appear partly altered as if they are relics of the host syenite, whereas others appear to be part of the vein assemblage (Fig. 5G). Such titanite II generally has higher Al, Fe, F and lower Ti than titanite I (cf. Che et al., 2013). Small euhedral zircon crystals are found either in or adjacent to the veins (Figs. 3B, 5G, I), Some chlorite + quartz veins are cut by epidote, late titanite and late Fe-oxide/hydroxide minerals that are also concentrated in veins.

The vein chlorite forms large euhedral crystals, some zoned from Fe-rich cores to Mg-rich rims and some with expanded cleavage planes (*a* in Fig. 3A). Some chlorite forms crystals in parallel orientation to scapolite (b in Fig. 3A) or as clots of radiating prismatic crystals cut by or filling open fractures. Chlorite thus formed in part during post solidus alteration and in part during hydrothermal activity.

This is a preprint, the final version is subject to change, of the American Mineralogist (MSA)
Cite as Authors (Year) Title. American Mineralogist, in press.
DOI: https://doi.org/10.2138/am-2019-6668

METHODS

SEM and Raman spectroscopy studies

Polished thin sections were prepared from each of nine samples of the syenite (Table 1), and examined by petrographic microscope. Carbon-coated polished thin sections were analyzed by Scanning Electron Microscope (SEM) located at the Regional Analytical Centre of Saint Mary's University (Appendices 1-3), acquiring back-scattered electron (BSE) images and energy dispersive spectroscopy (EDS) chemical analyses of minerals. The SEM used is a Tescan Mira 3 FESEM with a maximum resolution up to 1.2 nm at 30 kV. This SEM is also equipped with an INCA X-max 80 mm^2 silicon-drift detector EDS system, with a detection limit >0.1%. The SEM uses a tungsten filament to supply electrons to produce a BSE image of the grains on the polished thin section. Minerals in general are identified on the basis of their chemical composition compared with mineral compositions reported in the literature. Hydrous or carbonate mineral phases or those containing ferric iron (Fe^{3+}) were identified by inspection of un-normalized EDS data, with low totals corresponding to mineral structures containing water, CO_3^{2-}, and/or ferric iron. The identification of such minerals is described in more detail in Appendix 4 of Pe-Piper et al. (2017a). A reflected-light microscope was used to distinguish magnetite from hematite. The TiO_2 mineral polymorphs were distinguished by Raman laser spectroscopy, using a Horiba Jobin-Yvon LabRam HR confocal microscope (LRM) (Appendix 3 in Pe-Piper et al., 2018c). The LRM uses a 100mW 532 nm Nd-YAG diode laser from Toptica Phonotics and a Synapse charge-coupled device from Horiba Jobin-Yvon. The LRM also uses a 100x Olympus MPIaN objective lens for image analyses. The spectra were collected in one spectral window of 0-1600 cm^{-1}.

Selected locations in some samples were also used for elemental mapping of quantitative compositional data that were processed by the QuantMap package in Oxford Instrument's INCA program and reported as oxides. The color bar at the bottom of each elemental image is scaled to the corrected EDS analysis (volatile free). Mineral abbreviations follow Whitney and Evans (2010). The term Fe-oxide mixture (Fe-ox) is used to describe unresolved fine-grained mixtures of Fe-oxyhydroxides including hematite and goethite.

Laser ablation trace element analysis and U-Pb dating of rutile

Laser-ablation inductively coupled plasma mass spectrometry (LA-ICPMS) was carried out at the Department of Earth Sciences, University of New Brunswick-Fredericton on 30 μm thick polished thin sections**.** The instrument used is an Australian Scientific Instruments M-50 193nm ArF excimer laser ablation system (Compex Pro 110) connected to an Agilent 7700x ICP-MS.

Trace element analysis of rutile used a 33 μm spot size with energy of 5 J/cm^2 (laser fluence). The standards used were the NIST610 (for tuning) and NIST612 (primary standard) and BHVO and MKED titanite (Spandler et al.,2016) as secondary standards to check the accuracy of trace element measurements. An assumed stoichiometric value of 59% Ti in rutile was used for internal standardization. Gas flow rates were 930 ml/min for argon, 300 ml/min for ultra pure helium, and 2 ml/min for ultra pure nitrogen. The laser and ICP-MS are tuned using NIST610 to maximize sensitivity while also minimizing oxide production to <0.2% (as monitored by ThO^+/Th^+) and, for trace-element analyses, double-charged production to <0.3% (as monitored by $^{22}M^+/^{44}Ca^{++}$). These tuning conditions help minimize the most common isotope interferences. In

particular, there is no evidence for $^{(39,40)}$Ar-$^{(48,49)}$Ti interferences on ^{88}Sr and ^{89}Y based on accurate recovery of the latter elements in the BHVO glass and MKED titanite. The second rotary vacuum pump was also used, which increases the sensitivities of medium and heavy masses. A 30 s background with a 30 s ablation counting time was used.. During trace element analyses, Si and Ca were determined to make sure that rutile and titanite, which are texturally closely related, could be differentiated. Only analyses with <0.2 wt % SiO_2 and CaO are used.

Similar conditions were used for U-Pb dating of rutile, using primary standard R10 and secondary standard R13 (Luvizotto et al., 2009). The R13 rutile showed both normal and reverse discordance with the <1% discordant sub-group (n = 5/15) defining an age of 515 ± 6 Ma that overlaps the assumed ~510 Ma age of this material. Instrumental settings and calculation procedures are detailed by McFarlane (2015). Analytical spots with a 45 μm diameter were chosen from areas of rutile crystals appearing homogenous in BSE images, which were also used to identify if any Fe-oxide was present (Supp. Fig. S1). No zoning in rutile has been detected. Only near concordant analyses were used for Concordia age calculations; all but one (with 20 cps) had net ^{204}Pb <12 cps, which is less than the internal 2σ error. As a result, no common-Pb correction was applied and weighted mean ^{206}Pb/^{238}U ages were also calculated when appropriate. ^{208}Pb was measured but not used because the rutile standard has very low ^{232}Th and thus very large errors for the ^{208}Pb/^{232}Th system.

XRF maps (Fig. 3) used the Bruker M4 Tornado with a Rh X-ray tube, a working energy of 50 KV and 400 μA, and a scan speed of 6.5 mm/s. The color scale was

normalised to the maximum X-ray counts for Ti (rutile), Fe (magnetite), K (K-feldspar), Ca (calcite), and Si (quartz).

RUTILE MINERALOGY, GEOCHEMISTRY AND GEOCHRONOLOGY

Rutile morphology

Rutile in the syenite occurs in several forms:

1) As large magmatic prismatic crystals (up to 9 mm in length; Fig. 3A). The large rutile crystals are generally overgrown and partially replaced by titanite and then both are overgrown by Fe-oxide minerals, generally titanomagnetite. Thick titanite rims appears to have a reaction relationship with the rutile. These composite euhedral crystals have an interlocking texture with K-feldspar and scapolite (Fig. 3). In some cases only small remnants of rutile remain in the titanite, commonly aligned parallel to the prismatic form (Fig. 5A, B). The proportions of the three component minerals in the composite megacrysts is highly variable, with rutile ranging from trace amounts in titanite (*b* in Fig. 3B) to > 80% (Figs. 5C, 6A); titanite from <5% (Fig. 6A) to 60 % and magnetite generally between 20% and 40% (Fig. 3; 5A).

2) Smaller subhedral rutile crystals, typically 100 μm in size although exceptionally up to 1 mm, are little altered and only discontinuously rimmed by titanite that does not seem to show a reaction relationship (Fig. 5D, E). Their overall occurrence is interstitial within the K-feldspar (scapolite) framework, although some crystals include prismatic faces (Fig. 5D).

3) Other smaller rutile crystals are irregular (Fig 5F), apparently occupying late-magmatic pores in a largely crystalline mass of K-feldspar (now scapolite). Some have small crystals of titanite and less commonly magnetite at their margins.

Some crystals of rutile and rarely some titanite have exsolution lamellae of an Fe-rich phase, too small to analyse but presumably ilmenite or hematite (Fig. 5F). The presence of only rutile among the TiO_2 polymorphs was confirmed by Raman spectroscopy on all three types of grains of a range of sizes (Supp. Fig. S4).

The large prismatic composite grains are cut by fractures commonly orthogonal to the length of the crystal (Fig. 5B, C; 6A). Alteration along those fractures has resulted in complex intergrowths of magnetite and titanite II (Fig. 5B, C). These appear dark brown under plane polarized light (Supp. Fig. S6) and also extend into micron-scale fractures in the rutile.

Zr in rutile

Distribution of Zr in rutile and the host rock has been determined from XRF elemental mapping (Fig. 3B, 6B), which shows that Zr content of rutile is quite variable. Rastered abundance data for Zr were obtained by LA-ICPMS from four large composite prismatic grains (Supp. Fig. S5) and show domains with ~ 0.6% Zr (high-Zr rutile) and domains with ~0.2 % Zr (low-Zr rutile). Selected spots in grains > 100 μm were also analyzed by LA-ICPMS (Table 2; Fig. 7).

Where a large prismatic composite grain with a rutile core includes both high ad low-Zr domains, the high Zr domains occur preferentially at the outer rim of the rutile crystal (a in Fig. 6) and adjacent to fractures (b in Fig. 6), and in places the high-Zr domains are inhomogeneous (c in Fig. 6). Zr-rich crystallites 30–50 μm in size (d in Fig.

268 6) occur in veins comprising chlorite, calcite, titanite II, and analcime (Fig. 3B; 5G, H)
269 and in adjacent scapolite (Fig. 5I). Zircon crystallites appear to be absent from magnetite
270 overgrowths and in veins containing Fe-oxide mixture (Fig. 6B).

271 **Rutile geochronology**

272 Fifteen U-Pb dates close to Concordia and with reasonable errors (identified as
273 A–P, Fig. 8; Table 3) were obtained from 9 rutile grains. Five spots on interstitial grains
274 gave a Concordia age of 353.9 ± 5.7 Ma (Fig. 8A). Seven spots from domains in large
275 prismatic grains with Zr >0.3% gave a Concordia age of 337.4 ± 3.5 Ma (Fig. 8C). Only
276 three spots were from domains in prismatic grains with Zr <0.3%, yielding a Concordia
277 age of 348.1 ± 8.2 Ma (Fig. 8B), intermediate between the interstitial grains and the high-
278 Zr prismatic grains.

279 **Trace elements in rutile**

280 Three types of REE pattern are distinguished from rutile grains. Type 1 (Fig. 9A)
281 displays a decrease from normalized LREE to HREE with a negative Eu anomaly. LREE
282 are 1–100 times chondrite, HREE 0.5–10 times chondrite. Type 2 (Fig. 9B) displays a flat
283 REE pattern (LREE ~HREE) with LREE and HREE both 0.05–20 times chondrite, lower
284 than in Type 1. Type 3 (Fig. 9C) shows normalized HREE > LREE, most REE values
285 <0.2 times chondrite, higher Yb and Lu and many MREE below detection limit. Type 1
286 REE patterns are almost entirely in interstitial grains (Fig. 9A). Of the six spots analyzed
287 in the large prismatic crystal of Figure 6, five from high Zr domains (>2400 ppm) show
288 Type 3 REE patterns (Fig. 9C) and one from a low Zr domain (<700 ppm) is quite
289 different and of Type 2 (Fig. 9B).

Rutile with very low abundance of Zr (<600 ppm) has quite variable abundance of trace elements such as Nb, U and Th (Supp. Fig. S2). With increasing Zr content, only U shows a positive correlation with Zr (Fig. 10), whereas Ce, Th and Nb show an inverse relationship to Zr at higher Zr concentrations. Several elements including Ta and Yb show no clear relationship with Zr content.

DISCUSSION

Magmatic vs. hydrothermally altered rutile

Textural relationships of minerals suggest that there was more than one generation of rutile. The large prismatic rutile crystals, with a reaction rim of titanite 1 followed by titanomagnetite overgrowths (Figs. 3, 5, 6), are magmatic, because they show igneous textural relationships with feldspars and are found only in the pegmatitic syenite. Likewise, the larger interstitial rutile crystals (> 100 μm) with some euhedral faces are magmatic and may also have the titanite ± magnetite overgrowths. These large composite prismatic crystals are not present in the nearby gabbro and diorite bodies, which contain many of the alteration and vein minerals of the syenite, including scapolite, analcime, titanite II, chlorite, and quartz.

The high-Zr domains of the large prismatic crystals appear to be replacing a lower-Zr (500-600 ppm) grain, with preferential alteration at the margins of the grains and adjacent to fractures (Fig. 6), suggesting a hydrothermal origin. The hydrothermal origin of these domains is further supported by the following observations: a) U-Pb dating of such domains give younger ages with small errors (Fig. 8C); b) zircon is found in hydrothermal veins cutting scapolite (Fig. 5G, H) and c) small high-Zr crystallites

(~10-20 μm) also occur in hydrothermal scapolite adjacent to the veins (Figs. 3B; 5I; e in 6B). These latter two observations show that the hydrothermal event that produced the high-Zr rutile postdated the scapolite hydrothermal event. REE were leached from the hydrothermally altered Zr rich grains, which have low REE contents of Type 3, but U content appears to have increased, thus potentially resetting the U-Pb clock.

The presence of hydrothermal zircon in some veins suggests temperatures of at least 250 °C (Bojanowski et al. 2012). Chlorite geothermometry using the method of Cathelineau and Nieva (1985) suggests a maximum temperature for the veins of 190 °C (Pe-Piper et al., 2017a). No characteristically high-temperature minerals or mineral textures are present in the veins in syenite, or in other rocks of the Clarke Head megabreccia.

Geochronology of the syenite stock

The oldest rutile U-Pb dates are from smaller interstitial grains that have no evidence for hydrothermal alteration and collectively give a date of 353.9 ± 5.7 Ma (Fig. 8A). Large prismatic rutile crystals with Zr <0.3 % give a date of 348.1 ± 8.2 Ma, identical within error to interstitial grains (Fig. 8B). The date of the high-Zr hydrothermal rutile is 337.4 ± 3.5 Ma (Figs. 8C). Large crystals of magmatic rutile experienced partial Pb loss and/or U gain during hydrothermal alteration. The cluster of dates at ~337 Ma suggests that this represents the age of the hydrothermal alteration. The age of the initial intrusion was probably no younger than the precise concordant age of 360 Ma for rutile grain G (Fig. 8A) and certainly no younger than 353.9±5.7 Ma, the composite Concordia age of all interstitial grains.

The initial emplacement age for the syenite is similar to the ages for the younger intrusions in the A-type granite plutons of the Cobequid Highlands, which are dated between 365±4 Ma and 358 ±4 Ma (Dunning et al. 2002; Pe-Piper et al. 2004, 2018b). Sodic alteration with growth of albite and riebeckite in the West Moose River pluton (Fig. 1) is dated at about 355 ±4 Ma by $^{40}Ar/^{39}Ar$ from riebeckite (Pe-Piper et al. 2004).

The hydrothermal alteration event producing high-Zr rutile gives a concordant set of dates around 337 Ma. Based on the biostratigraphy of the Windsor Group (von Bitter et al. 2003; P.S. Giles, pers. comm. 2017), this age is towards the end of the ~8 Ma hiatus between the Lower Windsor Group, dominated by evaporites including halite, and the Upper Windsor Group in the nearby Kennetcook basin (Fig. 1a). Basin-margin deformation is a characteristic feature of Early Carboniferous basins of Nova Scotia (e.g. Hamblin and Rust 1989) and megablocks of gypsum and limestone from the lower Windsor Group are present at Clarke Head. It is therefore likely that hydrothermal fluids responsible for the Zr enrichment of rutile had access to Windsor Group halite. Basinal fluids buffered by halite deposits typically contain F^- abundance that is ~0.01% of Cl^- abundance (Worden 1996). This hydrothermal alteration of rutile is a little older than two lamprophyre dykes near the West Moose River pluton that both gave ages of ~334 Ma (Pe-Piper et al. 2018a).

Origin of the REE patterns in rutile

Type 3 REE patterns (Fig. 9C), with a U-shaped pattern with HREE>LREE and MREE least abundant, are characteristic of high-Zr rutile grains that give ages of ~337 Ma. The mineralogical control of this REE pattern is uncertain. In the granites of the Cobequid Highlands, LREE-enriched REE minerals predominate in both primary

(magmatic) and hydrothermal phases (Papoutsa and Pe-Piper 2013, 2015). The LREE enrichment decreasing to the MREE may thus reflect the greater availability of LREE in the hydrothermal system. The increasing normalized abundance of the HREE matches laboratory determinations of melt-rutile distribution coefficients for REE (Fig. 9D; Klemme et al. 2005).

Neither type 1 nor type 2 REE patterns (Figs. 9A, B) seem to be the result of magmatic crystallisation of rutile and are less clearly restricted to any one type of rutile grain and may be carried by micron-scale inclusions in the rutile (Supp. Fig. S3). The enrichment of type 1 REE patterns with LREE 1–100 times chondrite for La may relate to felsic melt inclusions similar to regional granites, which have La abundance at 100–1000 times chondrite levels (Papoutsa et al. 2016). The type 2 REE patterns with no Eu anomaly may be related to some other mineral inclusion that is richer in REE than rutile. The most likely candidate is ilmenite, with a rather flat normalized REE pattern (Villemant 1988; Nielsen et al. 1992). Ilmenite occurs as inclusions in rutile (Supp. Fig. 3B) and exsolution lamellae in rutile may be either ilmenite or hematite (Putnis and Wilson, 1978; Fig. 5F). Magmatic magnetite has a similar flat pattern but a slightly lower distribution coefficient with melt (Nielsen et al. 1992).

Magmatic evolution of rutile

Rutile tends to be stable at high temperatures and pressures and titanite at lower temperatures and pressures (Meinhold, 2010), with the stability fields strongly influenced by Ca content of magma (Angiboust and Harlov, 2017). It is presumably the very low Ca content of the original pristine syenite magma batches (predominantly K-feldspar, lesser albite) that favoured the precipitation of some magmatic rutile as interstitial grains late in

the crystallization history. Large prismatic rutile crystals with titanite overgrowths showing a reaction relationship (Fig. 6B) crystallized at depth and was brought up with the magma into the titanite stability field. With pressure and temperature decreasing, titanite precipitation was favored by an increase in Ca, presumably resulting from partial digestion of the gabbro blocks that are present in the syenite. Replacement of rutile by titanite I was a dissolution-precipitation process preferentially along the {110} cleavage of rutile, resulting in textures with residual blocks of rutile parallel to the prismatic crystal form (Fig. 5B). Evidence that much of the replacement of large prismatic rutile crystals by titanite was magmatic is that smaller interstitial rutile grains in the same sample (Fig. 3B) are not altered to titanite (e.g. rutile in Fig. 5F, compared to nearby large prismatic crystals shown in Fig. 3B).

Titanite forming a reaction rim around rutile is also known from exhumed high-pressure granulites (Carswell and O'Brien, 1993; Lucassen et al., 2011) and a block of gabbro granulite is reported from the Clarke Head megabreccia (Gibbons et al., 1996). However, we see no evidence of high-pressure minerals in the syenite that might support a xenocrystic high-pressure origin for the large rutile crystals and there is no evidence for exsolution of zircon crystallites in the rutile (Kelsey and Hand, 2015).

The Zr in rutile geothermometer (Tomkins et al. 2007; Liu et al. 2015) has been used for ultra-high-pressure eclogites and plutonic rocks and requires that quartz and zircon coexist as magmatic phases. Although both minerals are present in the Clarke Head syenite, neither is proven to be magmatic. The high-Zr rutile is clearly of hydrothermal origin. Application of the Tomkins et al. (2007) geothermometer for low (0.25 GPa) pressure conditions (Fig. 7) gives temperature estimates of ~550–650 °C for

low-Zr analyzed spots in rutile (Zr ~75–800 ppm; Table 3), that may represent magmatic temperature for the emplacement of syenite.

Fluid-aided alteration of rutile and Zr mobility

The large prismatic magmatic rutile crystals have experienced a variety of post-solidus fluid-aided dissolution and reprecipitation processes. These can be placed in a loose chronological framework through their relationship to the scapolitization of K-feldspar and the dated formation of Zr-rich hydrothermal rutile.

The large composite prismatic crystals of rutile-titanite-magnetite form an interlocking texture with similarly large K-feldspar crystals now replaced by scapolite (Fig. 3B, 4E). At least some of the replacement of rutile by more stable titanite and magnetite is probably a post-solidus process, as suggested by irregular distribution of residual rutile (Fig. 3B), the complex intergrown textures of magnetite and titanite with widespread porosity (top left of Fig. 5B; bottom right of Fig. 5C), and the development of small fractures in rutile hosting intergrown magnetite and titanite (Fig. 5C). The intergrown pattern shown by magnetite and titanite suggests 3D heterogeneous nucleation during coupled dissolution-precipitation (Ruiz-Agudo et al., 2014). The increasing proportion of magnetite on the rims of crystals (Fig. 5A, C) suggests that early dissolution-precipitation was dominated by magmatic fluids from the syenitic magma and then became increasingly influenced by alteration of the gabbro, where early veins of epidote have ~12% FeO_t content.

Parts of the syenite have irregular veins several mm wide of uncertain origin (Fig. 3A). Some appear bounded by euhedral scapolite grains replacing individual large K-feldspar grains (Fig. 5G). Others appear to cross-cut unaltered K-feldspar (*c* in Fig. 3A).

Some large composite rutile-titanite-magnetite grains appear to have been dissolved out and subsequently vein minerals have filled most of the void (Fig. 4E). The timing of these veins with respect to scapolitization is uncertain,

After scapolitization, some large prismatic rutile crystals were hydrothermally altered, preferentially along fractures, with the addition of high concentrations (>0.5%) of Zr. The geometry of the high-Zr domains (Fig. 6) precludes formation by overgrowth, requiring some type of dissolution-reprecipitation process. This was likely by a layer-by-layer mechanism (Ruiz-Agudo et al., 2014) given the mineralogical similarity of the orginal and reprecipitated phase, producing abrupt planar boundaries subparallel to fractures and crystal boundaries (Fig. 6B). Original inclusions in the rutile with LREE and HFSE were lost during this process. On the other hand, U appears to have been a significant component of the fluids, and the addition of U to the high-Zr domains (Fig. 10) is consistent with the observation that many of the high-Zr rutile grains have young dates ca. 337 Ma with small errors, suggesting that the growth of radiogenic Pb was dominated by the metasomatic addition of U during a single event.

Probable magmatic rutile grains with older U-Pb dates, generally as interstitial crystals, have low abundances of Zr (<800 ppm) and rather variable content of trace elements such as Nb, Th, and U (Fig. 10). This variability may result principally from inclusions within the rutile, such as ilmenite, magnetite and melt inclusions, as interpreted for type 1 and 2 REE patterns. The spread of older U-Pb dates implies variable Pb loss or U gain during the various hydrothermal processes that have altered the syenite.

448 The important role of halogens in the formation of rutile has been demonstrated
449 by experimental work in the temperature range 250–650 °C (e.g. Tanis et al., 2016). In
450 general, the influence of temperature in the hydrothermal range on mineral solubility is
451 small compared to the effect of fluid composition, especially halide concentration
452 (Knauss et al., 2001; Rapp et al., 2010; Wu and Koga, 2013), with F more effective than
453 Cl. As Ti^{4+} and Zr^{4+} have the same charge and the ionic radius of Zr^{4+} is only a little
454 larger (72 vs. 60.5 pm), the speciation between Ti and Zr with Cl, F, and OH is similar
455 (Griffith and Wickins, 1967; Pokrovski et al., 2013). That halogen-rich aqueous fluids
456 can dissolve, transport and precipitate significant quantities of HFSE is indicated by the
457 presence of rutile-bearing vein networks in blueschists and eclogites (John et al. 2008).
458 The widespread scapolititization of K-feldspar in the syenite involved large amounts of
459 Na^+ and Cl^-, for example as demonstrated for the Humboldt Lopolith in Nevada (Vanko
460 and Bishop 1982). Thus halogens were probably also implicated in the fluid-controlled
461 coupled dissolution-precipitation process that partly replaced the large prismatic rutile
462 crystals with high Zr rutile with type 3 REE (Fig. 9).
463 Halide complexing of Ti and Zr accounts for many of our observations.
464 Hydrothermal circulation enriched in halogens from the lower Windsor Group evaporites
465 first led to the alteration of K-feldspar to scapolite and the formation of scapolite-rich
466 veins with analcime (III) that cut both syenite and gabbro. These physicochemical
467 conditions increased the solubility of rutile and caused partial dissolution of the pre-
468 existing magmatic rutile and/or titanite (*a* in Fig. 3B; 4E), particularly along fractures
469 (large grain in Fig. 3A; 6). Hydrothermal zircon precipitated in and adjacent to veins of

analcime (III) that cut the scapolite, and a dissolution-precipitation process created domains of high Zr rutile in the existing rutile crystals.

IMPLICATIONS

We have shown that rutile can experience complex and varied coupled dissolution-precipitation reactions in shallow intrusions in the presence of halogens. The abundance of magmatic rutile in the Clarke Head syenite is a consequence of the back-arc setting of Devonian–Carboniferous magmatism in the Cobequid Highlands. Sub-continental lithospheric mantle (SCLM) was enriched in HFSE including Ti during Neoproterozoic subduction in the Avalon terrane (Murphy et al., 2008) and further enriched in Na, REE and halogens by Devonian subduction of the Rheic Ocean (Papoutsa et al., 2016). Partial melting of this SCLM produced magmas rich in Ti. The particular parent magma of the syenite was very depleted in Ca, thereby extending the stability field of rutile relative to titanite. Interstitial rutile crystallized at emplacement depths was resistant to subsequent dissolution-reprecipitation processes, but large rutile grains inferred to have formed at higher pressures and temperatures prior to feldspar crystallization were metastable at emplacement pressure and temperature and thus extremely susceptible to early dissolution-reprecipitation processes, either under late magmatic or post-solidus conditions. Dissolution of Ca and Fe from the adjacent gabbro blocks created the fluid conditions for 3D heterogeneous nucleation during coupled dissolution-precipitation. These processes were facilitated by the formation of fractures and porosity during the resulting volume changes as metastable high-temperature rutile was replaced by titanite. The likely enrichment of halogens in the magma, seen elsewhere

in Cobequid Highlands intrusions (Papoutsa et al., 2016) would have facilitated the coupled dissolution-precipitation process.

Some 15–20 million years after emplacement, a new phase of dissolution, some with coupled reprecipitation, took place. Permeability was enhanced by basin-margin faulting that also provided access to brines derived from halite deposits. These fluids largely converted K-feldspar to scapolite and albite to analcime. They are also inferred to have dissolved large prismatic grains of rutile and perhaps other HFSE minerals such as zircon. As halogen activity decreased as supply from fault-bound packets of halite was exhausted, layer-by-layer dissolution-reprecipitation of remaining large prismatic rutile grains resulted in high Zr contents (~5000 ppm) in the rutile, together with enrichment in U and depletion in high field strength elements.

Experimental studies suggest that rutile is not an important sink for REE except for the HREE (Klemme et al. 2005). Analyses of least altered magmatic rutile in this study suggests that most REE are in felsic melt inclusions or in exsolution lamellae or inclusions of ilmenite or an iron oxide, which also influence analyzed contents of other trace elements. Although trace element concentrations can be measured in both magmatic and hydrothermal rutile, their interpretation is complex.

ACKNOWLEDGEMENTS

This work was supported by a Discovery Grant 2016-04310 from the Natural Sciences and Engineering Research Council of Canada to GPP. We thank Brandon Boucher for the laser analytical work, Xiang Yang for his help with SEM work, and Thomas Zack and Dan Harlov for constructive comments on earlier drafts of this manuscript.

REFERENCES CITED

Altree-Williams, A., Pring, A., Ngothai, Y. and Brugger, J. (2015) Textural and compositional complexities resulting from coupled dissolution–reprecipitation reactions in geomaterials. Earth-Science Reviews, 150, 628–651.

Andersen, T. (2002) Correction of common lead in U–Pb analyses that do not report ^{204}Pb. Chemical Geology, 192, 59–79.

Angiboust, S. and Harlov, D. (2017) Ilmenite breakdown and rutile-titanite stability in metagranitoids: Natural observations and experimental results. American Mineralogist, 102(8), 1696−1708.

Audetat, A. and Keppler, H. (2005) Solubility of rutile in subduction zone fluids as determined by experiments in the hydrothermal diamond anvil cell. Earth and Planetary Science Letters, 232, 393–402.

Bojanowski, M.J., Bagiński, B., Clarkson, E., Macdonald, R., and Marynowski, L. (2012) Low-temperature zircon growth related to hydrothermal alteration of siderite concretions in Mississippian shales, Scotland. Contributions to Mineralogy and Petrology, 164(2), 245–259.

Carswell, D.A. and O'brien, P.J. (1993) Thermobarometry and geotectonic significance of high-pressure granulites: examples from the Moldanubian Zone of the Bohemian Massif in Lower Austria. Journal of Petrology, 34(3), 427−459.

Cathelineau, M. and Nieva, D. (1985) A chlorite solid solution geothermometer: the Los Azufres (Mexico) geothermal system. Contributions to Mineralogy and Petrology, 91(3), 235–244.

Che, X.D., Linnen, R.L., Wang R.C,, Groat, L.A., and Brand A.A. (2013) Distribution of trace and rare earth elements in titanite from tungsten and molybdenum deposits in Yukon and British Columbia, Canada. The Canadian Mineralogist, 51(3), 415–438.

Clarke, D.B., MacDonald, M.A., and Tate, M.C. (1997) Late Devonian mafic-felsic magmatism in the Meguma zone, Nova Scotia. in: The Nature of Magmatism in the Appalachian Orogen. Geological Society of America Memoir 191, 107–127.

Donohoe, H.V. Jr and Wallace, P.I. (1985) Repeated orogeny, faulting and stratigraphy of the Cobequid Highlands, Avalon Terrane of northern Nova Scotia. Geological Association of Canada- Mineralogical Association of Canada Joint Annual Meeting, Guidebook 3, Fredericton, N.B., 77 p.

Dunning, G.R., Barr, S.M., Giles, P.S., McGregor, D.C., Pe-Piper, G., and Piper, D.J.W. (2002) Chronology of Devonian to early Carboniferous rifting and igneous activity in southern Magdalen Basin based on U-Pb (zircon) dating. Canadian Journal of Earth Sciences, 39(8), 1219–1237.

Foley, S.F., Barth, M.G., and Jenner, G.A. (2000) Rutile/melt partition coefficients for trace elements and an assessment of the influence of rutile on the trace element characteristics of subduction zone magmas. Geochimica et Cosmochimica Acta, 64, 933–938.

Foley, S.F., Tiepolo, M., and Vannucci, R. (2002) Growth of early continental crust controlled by melting of amphibolite in subduction zones. Nature, 417, 837–840.

557 Gibbons, W. and Murphy, J.B. (1995) Mylonitic mafic granulite in fault megabreccia at
558 Clarke Head, Nova Scotia: a sample of Avalonian lower crust?. Geological
559 Magazine, 132, 81–90.
560 Gibbons, W., Doig, R., Gordon, T., Murphy, J.B., Reynolds, P. and White, J.C. (1996)
561 Mylonite to megabreccia: tracking fault events within a transcurrent terrane
562 boundary in Nova Scotia, Canada. Geology, 24, 411–414.
563 Griffith, W.P. and Wickins, T.D. (1967) Raman studies on species in aqueous solutions.
564 Part II. Oxy-species of metals of groups VI_A , V_A , and IV_A. Journal of the
565 Chemical Society, A, 1967, 675–679.
566 Hamblin, A.P. and Rust, B.R. (1989) Tectono-sedimentary analysis of alternate-polarity
567 half-graben basin-fill successions: Late Devonian-Early Carboniferous Horton
568 Group, Cape Breton Island, Nova Scotia. Basin Research, 2(4), 239–255.
569 Hayden, L.A. and Manning C.E. (2011) Rutile solubility in supercritical $NaAlSi_3O_8$
570 fluids, Chemical Geology, 284, 74–81.
571 Hibbard, J. and Waldron, J.W.F. (2009) Truncation and translation of Appalachian
572 promontories: Mid-Paleozoic strike-slip tectonics and basin
573 initiation. Geology, 37, 487–490.
574 John, T., Klemd, R., Gao, J. and Garbe-Schönberg, C.D. (2008) Trace-element
575 mobilization in slabs due to non steady-state fluid–rock interaction: constraints
576 from an eclogite-facies transport vein in blueschist (Tianshan, China). Lithos,
577 103(1), 1–24.

John, T., Scambelluri, M., Frische, M., Barnes, J.D. and Bach, W. (2011) Dehydration of subducting serpentinite: implications for halogen mobility in subduction zones and the deep halogen cycle. Earth and Planetary Science Letters, 308, 65–76.

Kelsey, D.E. and Hand, M. (2015) On ultrahigh temperature crustal metamorphism: Phase equilibria, trace element thermometry, bulk composition, heat sources, timescales and tectonic settings. Geoscience Frontiers, 6(3), 311–356.

Klemme, S., Prowatke, S., Hametner, K., and Günther, D. (2005) Partitioning of trace elements between rutile and silicate melts: implications for subduction zones. Geochimica et Cosmochimica Acta, 69, 2361–2371.

Knauss, K.G., Dibley, M.J., Bourcier, W.L., and Shaw, H.F. (2001) Ti(IV) hydrolysis constants derived from rutile solubility measurements made from 100 to 300 °C. Applied Geochemistry, 9-10, 1115–1128.

Liu, Y.-C., Deng, L.-P., Gu, X.-F., Groppo, C., and Rolfo, F. (2015) Application of Ti-in-zircon and Zr-in-rutile thermometers to constrain high-temperature metamorphism in eclogite from the Dabie orogen, central China. Gondwana Research, 27, 410–423.

Lucassen, F., Franz, G., Dulski, P., Romer, R.L. and Rhede, D. (2011). Element and Sr isotope signatures of titanite as indicator of variable fluid composition in hydrated eclogite. Lithos, 121, 12−24.

Luvizotto, G.L., Zack, T., Meyer, H.P., Ludwig, T., Triebold, S., Kronz, A., Münker, C., Stockli, D.F., Prowatke, S., Klemme, S. and Jacob, D.E. (2009). Rutile crystals as potential trace element and isotope mineral standards for microanalysis. Chemical Geology, 261, 346–369.

MacInnes, E.A. and White, J.C. (2004) Geometric and kinematic analysis of a transpression terrane boundary: Minas fault system, Nova Scotia, Canada. Geological Society of London Special Publication, 224, 201–214.

McFarlane, C.R. (2015) A geochronological framework for sedimentation and Mesoproterozoic tectono-magmatic activity in lower Belt–Purcell rocks exposed west of Kimberley, British Columbia. Canadian Journal of Earth Sciences, 52(7), 444–465.

Meinhold, G. (2010) Rutile and its application in earth sciences. Earth Science Reviews, 102, 1–28.

Manning, C.E. (2004) The chemistry of subduction-zone fluids. Earth and Planetary Science Letters, 223, 1–16.

Murphy, J.B., Dostal, J. and Keppie, J.D. (2008) Neoproterozoic–Early Devonian magmatism in the Antigonish Highlands, Avalon terrane, Nova Scotia: tracking the evolution of the mantle and crustal sources during the evolution of the Rheic Ocean. Tectonophysics 461, 181–201.

Murphy, J.B., Waldron, J.W.F., Kontak, D.J., Pe-Piper, G., and Piper, D.J.W. (2011) Minas Fault Zone: Late Paleozoic history of an intra-continental orogenic transform fault in the Canadian Appalachians. Journal of Structural Geology, 33(3), 312–333.

Nielsen, R.L., Gallahan, W.E., and Newberger, F. (1992) Experimentally determined mineral-melt partition coefficients for Sc, Y and REE for olivine, orthopyroxene, pigeonite, magnetite and ilmenite. Contributions to Mineralogy and Petrology, 110(4), 488–499.

624 Owen, J.V. and Greenough, J.D. (1999) Scapolite pegmatite from the Minas fault, Nova
625 Scotia.: tangible manifestation of Carboniferous, evaporite-derived hydrothermal
626 fluids in the western Cobequid Highlands? Mineralogical Magazine, 63, 387–397.
627 Papoutsa, A. D. and Pe-Piper, G. (2013) The relationship between REE-Y-Nb-Th
628 minerals and the evolution of an A-type granite, Wentworth Pluton, Nova Scotia.
629 American Mineralogist, 98(2-3), 444–462.
630 Papoutsa, A. and Pe-Piper, G. (2015) Variation of REE-hydrothermal circulation in
631 complex shear zones: The Cobequid Highlands, Nova Scotia. The Canadian
632 Mineralogist, 52, 943–968.
633 Papoutsa, A., Pe-Piper, G., and Piper, D.J.W. (2016) Systematic mineralogical diversity
634 in A-type granitic intrusions: Control of magmatic source and geological
635 processes. Geological Society of America Bulletin, 128(3-4), 487–501.
636 Pe-Piper, G. and Piper, D.J.W. (2003) A synopsis of the geology of the Cobequid
637 Highlands, Nova Scotia. Atlantic Geology, 38, 145–160.
638 Pe-Piper, G., Reynolds, P.H., Nearing, J., and Piper, D.J.W. (2004) Evolution of a Late
639 Paleozoic shear zone in the Cobequid Highlands, Nova Scotia: an $^{40}Ar/^{39}Ar$
640 geochronology study. Canadian Journal of Earth Sciences, 41, 1425–1436.
641 Pe-Piper, G., Nagle, J., and Piper, D.J.W. (2017a) Igneous rocks and hydrothermal
642 alteration of Lower Carboniferous sedimentary rocks, Clarke Head, Minas Fault
643 Zone, western Nova Scotia. Geological Survey of Canada Open File 8314.
644 Pe-Piper, G., Piper, D.J.W., Papoutsa, A., and Wisen, J. (2017b) The fractured latest
645 Devonian granites of the West Moose River Pluton along the Cobequid Shear

646 Zone, Nova Scotia: implications for regional mineralisation. Canadian Journal of
647 Earth Sciences, 54(11), 1119–1137.
648 Pe-Piper, G., Piper, D. J.W., and Papoutsa, A. (2018a) Mid Carboniferous lamprophyres,
649 Cobequid Fault Zone, eastern Canada, linked to sodic granites, voluminous
650 gabbro, and albitization. Lithos, 296, 316–331.
651 Pe-Piper, G., Piper, D. J.W., McFarlane, C. R., Sangster, C., Zhang, Y., and Boucher, B.
652 (2018b). Petrology, chronology and sequence of vein systems: Systematic
653 magmatic and hydrothermal history of a major intracontinental shear zone,
654 Canadian Appalachians. Lithos, 304, 298–310.
655 Pe-Piper, G., Nagle, J., and Piper, D.J.W. (2018c) Mineralogical details of igneous rocks
656 from Clarke Head, Minas Fault Zone. Geological Survey of Canada Open File
657 (submitted)
658 Pokrovski, G.S., Borisova, A.Y., and Bychkoy, A.Y. (2013) Speciation and transport of
659 metals and metalloids in geological vapors. Reviews of Mineralogy and
660 Geochemistry, 76,165–218.
661 Putnis, A. and Wilson, M.M. (1978) A study of iron-bearing rutiles in the paragenesis
662 TiO_2-Al_2O_3-P_2O_5-SiO_2. Mineralogical Magazine, 42 (322), 255–263.
663 Rapp, J.R., Klemme, S., Butler, I.B., and Harley, S.L. (2010) Extremely high solubility of
664 rutile in chloride and fluoride-bearing metamorphic fluids: an experimental
665 investigation. Geology, 38, 323–326.
666 Ruiz-Agudo, E., Putnis, C.V. and Putnis, A. (2014) Coupled dissolution and precipitation
667 at mineral–fluid interfaces. Chemical Geology, 383, 132–146.

668 Ryerson, F.Y. and Watson, E.B. (1987) Rutile saturation in magmas: implications for Ti,
669 Nb, Ta depletion in island-arc basalts. Earth and Planetary Science Letters 86,
670 225–239
671 Spandler, C., Pettke, T., and Rubatto, D. (2011) Internal and external fluid sources for
672 eclogite-facies veins in the Monviso meta-ophiolite, Western Alps: implications
673 for fluid flow in subduction zones. Journal of Petrology, 52, 1207–1236.
674 Spandler, C., Hammerli, J., Sha, P., Hilbert-Wolf, H., Hu, Y., Roberts, E., and Schmitz,
675 M. (2016). MKED1: a new titanite standard for in situ analysis of Sm–Nd
676 isotopes and U–Pb geochronology. Chemical Geology, 425, 110–126.
677 Tanis, E.A., Simon, A.C., Tschauner, O., Chow, P., Xiao, Y., Burnley, P., Cline, C.J.,
678 Hanchar, J.M., Pettke, T., Shen, G., and Zhao, Y. (2015) The mobility of Nb in
679 rutile-saturated NaCl-and NaF-bearing aqueous fluids from 1–6.5 GPa and 300–
680 800 °C. American Mineralogist, 100(7), 1600–1609.
681 Tanis, E.A., Simon, A., Zhang, Y., Chow, P., Xiao, Y., Hanchar, J.M., Tschauner, O.,
682 and Shen, G. (2016) Rutile solubility in NaF-NaCl-KCl-bearing aqueous fluids at
683 0.5–2.79 GPa and 250–650 °C. Geochimica et Cosmochimica Acta, 177,170–181.
684 Tomkins, H.S., Powell, R., and Ellis, D.J. (2007) The pressure dependence of the
685 zirconium-in-rutile thermometer. Journal of Metamorphic Geology, 25, 703–713.
686 Tropper, P. and Manning, C.F. (2005) Very low solubility of rutile in H_2O at high
687 pressure and temperature, and its implications for Ti mobility in subduction
688 zones. American Mineralogist, 90, 502–550.

689 Vanko, D.A. and Bishop, F.C. (1982) Occurrence and origin of marialitic scapolite in the
690 Humboldt Lopolith, NW Nevada. Contributions to Mineralogy and Petrology,
691 81(4), 277–289.
692 von Bitter, P.H., Giles, P.S., and Utting, J. (2003) Biostratigraphic correlation of major
693 cycles in the Windsor and Codroy groups of Nova Scotia & Newfoundland,
694 Atlantic Canada, with the Mississippian substages of Britain and Ireland. In: Proc
695 XVth International Congress of Carboniferous and Permian Stratigraphy, Utrecht,
696 The Netherlands, 10–16.
697 Villemant, B. (1988) Trace element evolution in the Phlegrean Fields (Central Italy):
698 fractional crystallization and selective enrichment. Contributions to Mineralogy
699 and Petrology, 98(2), 169–183.
700 Whitney, D.L. and Evans, B.W. (2010) Abbreviations for names of rock-forming
701 minerals. American Mineralogist, 95,185–187.
702 Worden, R.H. (1996) Controls on halogen concentrations in sedimentary formation
703 waters. Mineralogical Magazine, 60, 259–274.
704 Wu, J. and Koga, K. (2013) Fluorine partitioning between hydrous minerals and aqueous
705 fluid at 1 GPa and 770-947 °C: a new constraint on slab flux. Geochimica et
706 Cosmochimica Acta, 119, 77–92.
707 Zack, T., Kronz, A., Foley, S.E., and Rivers, T. (2002) Trace element abundances in
708 rutiles from eclogites and associated garnet mica schists. Chemical Geology, 184,
709 97–122.

This is a preprint, the final version is subject to change, of the American Mineralogist (MSA)
Cite as Authors (Year) Title. American Mineralogist, in press.
DOI: https://doi.org/10.2138/am-2019-6668

FIGURE CAPTIONS

Figure 1: (a) Geological map of the Minas Fault Zone and surrounding terranes in southeastern Canada, showing location of Clarke Head. CF = Cobequid Fault; CSZ = Cobequid Shear Zone; KF = Kirkhill Fault; RBF = Rockland Brook Fault; WMRP = West Moose River Pluton. (b) Location of igneous rocks in the cliff section at Clarke Head.

Figure 2: (A) Field photograph of syenite close to gabbro contact, with hybrid monzonite at the contact, partly digested gabbro xenoliths, and variable alteration of the syenite. (B) Photograph of syenite hand specimen showing coarse-grained texture with vugs.

Figure 3: XRF composite elemental maps of thin sections of syenite with K-feldspar largely replaced by scapolite and analcime. (**A**) Syenite cut by irregular fractures partly filled by calcite, quartz and chlorite. a = chlorite with expanded cleavage planes, b = chlorite parallel to margins of scapolite crystals, c = fracture cuts unaltered K-feldspar. Large rutile-titanite-magnetite prismatic crystal is shown in Fig. 6. (**B**) Syenite with several prismatic crystals of rutile-titanite-magnetite and common small irregular interstitial rutile grains, one shown in Fig. 5D. a = prismatic rutile-titanite-magnetite crystal apparently partly dissolved and pseudomorphed by quartz + calcite + analcime; b = titanite-magnetite prismatic crystal with minor rutile; gold * indicates high Zr spot.

Figure 4: Representative BSE images of scapolitization of syenite from sample 9928a. **A**: Analcime I forms interlocking crystals with K-feldspar and albite. a = analcime II fills a fracture in K-feldspar. **B**: Scapolite appears to have replaced K-

feldspar. Analcime appears to have replaced the albite lamellae in the K-feldspar (perthite) crystal. **C**: Scapolite vein cross-cuts calcite, K-feldspar, analcime I, and albite. **D**: A large K-feldspar crystal is partly replaced by scapolite and cross-cut by analcime II and quartz. **E**: Pseudomorph of an original rutile-titanite-magnetite prismatic grain, largely replaced by quartz, calcite and analcime.

Figure 5: Representative BSE images of rutile. **A:** Small rutile-titanite-magnetite prismatic crystal with large titanomagnetite overgrowth. [9956a] **B:** Zoom of 5A showing that rutile is largely replaced and overgrown by titanite and magnetite. Remnants of rutile are parallel to the prismatic form of the crystal. C: Prismatic rutile crystal, with thin rim of titanite and magnetite that has also invaded fractures in the rutile, Red spot has Zr = 14 ppm [9956c]. **D:** Small subhedral rutile crystal with some prismatic faces and small patchy overgrowths of titanite [9956a]. **E**: Interstitial rutile crystal overgrown at one end by discontinuous titanite and magnetite [9956d]. **F:** Interstitial rutile crystal with very small patchy titanite overgorwths. Exsolution lamellae of an Fe-rich mineral, probably hematite or ilmenite [9928a]. **G**: Quartz-analcime-titanite II vein cutting scapolite. Zircon grain (zoom in panel H) in the vein and smaller zircon crystallites in the scapolite [9928a]. **H**: Detail of zircon with hematite rim from panel G. **I**: Titanite-analcime vein cutting scapolite with 30 mm zircon adjacent to the vein [9928b].

Figure 6: A: XRF multi-element normalized map for a large prismatic rutile grain from sample 9956c (Fig. 3A). Details for the positions a–e are discussed in the text. **B**: XRF normalized map for Zr. The background speckled effect is an artefact of Si

interference with the Zr peak. I–M are locations of U-Pb geochronology (Table 2).

Figure 7: A: Plot of variation of Zr content with morphological type of rutile grain. Also shows corresponding temperature (°C) based on the Zr in rutile thermometer, calculated at 0.25 GPa as in Tomkins et al. (2007).

Figure 8: U-Pb Concordia diagrams and inverse $^{207}Pb/^{206}Pb$ isochron ages from rutile grains in the syenite. **A**: Interstitial grains; **B**: Prismatic grains with low Zr; **C**: Prismatic grains with high Zr. Composite age statistics calculated using Isoplot. A–P are individual dated spots identified in Table 2 and Supplementary Figure S1.

Figure 9: REE patterns for rutile grains from the syenite (samples 9956a, b, c, d). **A**: Type 1 REE pattern, displaying an igneous trend with a negative Eu anomaly. **B**: Type 2 REE pattern, displaying a flat REE pattern with LREE≈HREE. **C**: Type 3 REE pattern, with low MREE and REE>LREE). **D:** Plot from data of Klemme et al. (2005) of REE concentrations in rutile crystallized in the laboratory.

Figure 10: Bi-plot of U vs Zr, based on LA-ICPMS data from various rutile grains (Table 2).

TABLES

Table 1. Summary of the studied samples.

Table 2. LA-ICPMS trace element analyses of rutile

Table 3. Analytical details of dated spots in rutile

This is a preprint, the final version is subject to change, of the American Mineralogist (MSA)
Cite as Authors (Year) Title. American Mineralogist, in press.
DOI: https://doi.org/10.2138/am-2019-6668

SUPPLEMENTARY FIGURES

Supplementary Figure S1: BSE images of all analyzed grains for geochronology. The letters indicate the analyses in Table 3 as well as Figure 7. Yellow outline indicates high Zr domain in panel (G) (cf. Fig. 6).

Supplementary Figure S2: Variation of trace elements with Zr in rutile, determined by LA-ICPMS (Table 2).

Supplementary Figure S3: Mineral inclusions in rutile. High backscatter inclusion has 46% TiO_2 and 44% FeO and is probably ilmenite, but possibly magnetite (with analysed TiO_2 from the rutile). Low backscatter spots in panel C may be voids. EDS analyses in Supplementary Table 1.

Supplementary Figure S4 Raman spectra for representative rutile grains confirming the presence of rutile.

Supplementary Figure S5. Raster data of Zr content (red graph, green scale in ppm) in four rutile grains from samples 9956b, 9956c, and 9956d. Also shows location of U-Pb geochronology spots (cyan) and trace element geochemical spots (magenta). The high-Zr domains are outlined in yellow in panel (C).

Supplementary Figure S6. Microphotograph of part of the large rutile grain in Fig. 6. The dark brown domains show a set of almost perpendicular striations (positions a). High-Zr domains are outlined in yellow.

Supplementary Figure S7. (A) Microphotograph (ppl) of complex rutile-titanite-magnetite grains that have grown in a vug bounded by large scapolite (pseudomorphing K-feldspar) crystals, and is thus late magmatic or post-solidus. (B). BSE image with spot analyses of one grain from panel (A) showing textural relationships between minerals.

Supplementary Table 1. Normalized wt.% oxides for the EDS analyses of inclusions in rutile in Supplementary Figure S3.

TABLE 1. Summary of the lithology and mineralogy of the samples studied in detail.

Sample	Lithology description	Minerals present
9956a	Pegmatitic patch of scapolitized syenite	Anl, Chl, Ep, Kfs, Py, Scp, Ttn, Rt
9956b		Ab, Anl, Cal, Chl, Py, Qz, Scp, Ttn, Rt, Zrn
9956c		Anl, Chl, Ep, Scp, Ttn, Rt
9956d		Anl, Chl, Qz, Scp, Ttn, Rt
9928a	Main phase of scapolitized syenite	Anl, Cal, Rt, Scp, Ttn
9928b		Ab, Anl, Kfs, Qz, Rt, Scp, Ttn, Zrn

Notes: Mineral abbreviations: Ab=albite, Anl=analcime, Cal=calcite, Chl=chlorite, Ep=epidote, Kfs=K-feldspar, Py=pyrite, Qz=quartz, Rt=rutile, Scp=scapolite, Ttn=titanite, Zrn=zircon.
All samples contain Fe oxides/hydroxides

Sample locality 45° 22.690' N 64° 14.983' W

TABLE 2. LA-ICPMS trace element analyses of rutile

Sample	Position	Habit[a]	Ti (cps) x10^{-3}	SiO_2 (wt %)	CaO (wt %)	Trace elements (ppm)																								
						Sr	Y	Zr	Nb	Sn	ΣREE	La	Ce	Pr	Nd	Sm	Eu	Gd	Tb	Dy	Ho	Er	Tm	Yb	Lu	Hf	Ta	W	Pb	Th	U
9928b	OG8	Int.	16730	b.d.[b]	0.03	1.12	0.10	18	223	17.5	b.d.	b.d.	b.d.	b.d.	b.d.	b.d.	b.d.	b.d.	b.d.	b.d.	b.d.	b.d.	b.d.	b.d.	0.6	4.5	15.6	0.02	b.d.	0.1
9956a	1	Int.	17610	0.03	b.d.	0.94	0.08	38	806	20.8	b.d.	b.d.	b.d.	b.d.	b.d.	b.d.	b.d.	b.d.	b.d.	b.d.	b.d.	b.d.	b.d.	b.d.	b.d.	2.7	28.7	0.8	0.03	0.29	1.3
9956a	15	Prsm	17970	b.d.	0.04	4.87	0.24	5	39	3.2	0.06	b.d.	b.d.	b.d.	b.d.	b.d.	b.d.	b.d.	b.d.	b.d.	b.d.	0.03	b.d.	0.03	b.d.	0.2	0.8	3.1	0.22	0.18	0.4
9956a	16	Prsm	18100	b.d.	0.05	6.59	0.35	4	33	3.1	0.10	b.d.	b.d.	b.d.	b.d.	b.d.	b.d.	0.02	b.d.	0.03	b.d.	0.03	b.d.	0.02	b.d.	0.2	0.6	1.5	0.23	0.64	0.7
9956a	18	Prsm	18210	0.04	0.06	6.20	0.22	15	44	3.2	0.11	b.d.	b.d.	b.d.	0.02	b.d.	b.d.	0.02	b.d.	b.d.	b.d.	0.03	b.d.	0.03	b.d.	0.4	1.4	14.5	0.62	0.16	0.3
9956a	60	Int.	17030	0.02	0.02	2.08	7.97	234	1328	157.7	94.0	18.0	41.2	4.8	18.3	3.5	0.3	2.9	0.4	2.0	0.4	1.1	0.1	1.0	0.2	16.8	67.0	44.2	0.5	8.6	167.0
9956a	61	Int.	16240	0.15	0.10	3.62	7.20	78	726	99.9	75.1	16.1	31.9	3.6	14.1	2.6	0.2	2.0	0.3	1.8	0.4	0.9	0.1	0.9	0.1	4.8	26.9	13.0	0.5	6.1	62.3
9956a	74	Prsm	16000	0.09	0.03	8.27	0.15	2	114	4.0	0.03	b.d.	b.d.	b.d.	b.d.	b.d.	b.d.	b.d.	b.d.	b.d.	b.d.	b.d.	b.d.	0.03	b.d.	0.1	4.3	3.1	0.54	0.12	0.2
9956b	11	Int.	16400	0.16	0.05	2.05	0.71	6500	908	26.4	0.81	0.13	0.21	0.03	0.08	0.07	b.d.	0.07	b.d.	0.10	0.02	0.07	b.d.	0.04	b.d.	191.2	33.8	1.5	0.11	0.81	26.7
9956b	19	Prsm	17400	b.d.	b.d.	1.43	0.22	2369	388	18.7	0.25	0.03	0.09	b.d.	b.d.	b.d.	b.d.	b.d.	b.d.	0.02	b.d.	0.02	b.d.	0.06	0.02	59.2	6.5	0.3	0.35	0.02	5.5
9956b	20	Prsm	16600	0.04	b.d.	0.76	0.13	6347	840	35.1	0.05	b.d.	b.d.	b.d.	b.d.	b.d.	b.d.	b.d.	b.d.	b.d.	b.d.	b.d.	b.d.	0.04	0.02	185.8	31.2	2.3	0.04	b.d.	40.8
9956b	33	Int.	16740	0.16	0.07	0.99	0.30	31	284	117.8	0.14	0.04	0.05	b.d.	b.d.	b.d.	b.d.	b.d.	b.d.	0.03	b.d.	0.02	b.d.	b.d.	b.d.	2.0	8.4	0.7	0.24	b.d.	0.7
9956b	34	Int.	17440	0.03	b.d.	0.82	0.16	38	248	127.0	0.10	b.d.	0.05	b.d.	0.02	b.d.	b.d.	b.d.	b.d.	0.03	b.d.	0.02	b.d.	b.d.	b.d.	1.8	10.3	0.4	0.07	0.02	1.1
9956b	65	Int.	16920	0.04	0.02	1.54	0.34	3390	1709	30.1	2.53	0.56	1.16	0.12	0.47	0.05	0.02	0.03	b.d.	0.06	b.d.	0.04	b.d.	0.02	b.d.	112.3	120.9	1.9	0.20	0.52	11.0
9956c	1	Prsm	16080	b.d.	0.02	9.40	0.08	b.d.	4	1.9	b.d.	b.d.	b.d.	b.d.	b.d.	b.d.	b.d.	b.d.	b.d.	b.d.	b.d.	b.d.	b.d.	b.d.	b.d.	b.d.	0.2	1.6	0.29	0.10	0.2
9956c	9	Prsm	16610	0.06	0.10	5.98	4.39	660	396	50.9	9.78	1.02	2.44	0.35	1.65	0.62	0.19	1.05	0.16	1.08	0.22	0.45	0.07	0.42	0.05	25.2	17.0	55.7	0.22	3.42	38.4
9956c	11	Prsm	16230	0.03	b.d.	0.86	0.12	2485	471	18.2	0.06	b.d.	b.d.	b.d.	b.d.	b.d.	b.d.	b.d.	b.d.	0.02	b.d.	b.d.	b.d.	0.04	b.d.	84.2	17.4	0.4	b.d.	b.d.	5.4
9956c	21	Prsm	16050	0.04	b.d.	0.86	0.08	5030	1267	29.5	0.03	b.d.	b.d.	b.d.	b.d.	b.d.	b.d.	b.d.	b.d.	b.d.	b.d.	0.02	b.d.	0.02	b.d.	130.1	22.3	8.4	0.04	0.03	40.4
9956c	22	Prsm	16270	0.04	b.d.	0.78	0.06	4229	1016	28.6	b.d.	b.d.	b.d.	b.d.	b.d.	b.d.	b.d.	b.d.	b.d.	b.d.	b.d.	b.d.	b.d.	b.d.	b.d.	118.8	23.9	3.6	b.d.	b.d.	20.9
9956c	23	Prsm	16190	b.d.	0.02	2.96	0.12	6396	959	35.6	0.09	b.d.	0.06	b.d.	b.d.	b.d.	b.d.	b.d.	b.d.	b.d.	b.d.	b.d.	b.d.	0.02	0.02	177.1	29.8	3.7	0.36	b.d.	43.4
9956c	24	Prsm	16380	0.09	b.d.	1.18	0.39	5630	785	32.0	0.58	0.11	0.21	b.d.	0.03	b.d.	b.d.	0.03	b.d.	0.07	b.d.	0.05	b.d.	0.06	0.02	156.9	27.5	2.4	0.09	0.03	37.6
9956c	29	Prsm	16640	b.d.	0.02	0.87	0.34	14	177	38.7	0.82	0.14	0.27	0.05	0.10	0.05	0.02	0.08	b.d.	0.08	b.d.	0.02	b.d.	0.02	b.d.	0.6	16.3	2.3	0.06	0.54	5.3
9956c	38	Int.	16180	b.d.	b.d.	0.75	0.06	1919	301	25.1	0.03	b.d.	b.d.	b.d.	b.d.	b.d.	b.d.	b.d.	b.d.	b.d.	b.d.	b.d.	b.d.	0.03	b.d.	59.0	8.7	0.4	0.03	0.03	7.6
9956c	45	Int.	16390	0.03	b.d.	1.65	2.67	326	677	124.3	29.3	5.8	12.8	1.5	5.4	0.9	0.1	0.9	0.1	0.7	0.1	0.4	0.1	0.4	0.1	17.0	35.3	20.5	0.9	4.1	53.4
9956c	58	Int.	15940	0.05	b.d.	1.19	0.23	4670	1466	36.2	1.79	0.33	0.84	0.09	0.32	0.05	b.d.	0.04	b.d.	0.03	b.d.	0.02	b.d.	0.08	b.d.	158.5	61.2	6.4	0.08	0.48	26.6
9956c	72	Int.	15870	0.05	0.04	2.88	1.27	413	2646	63.2	9.62	1.82	4.04	0.43	1.87	0.23	0.02	0.38	0.04	0.27	0.06	0.17	0.03	0.24	0.02	18.5	77.1	7.7	0.76	2.25	21.8
9956c	75	Int.	15760	0.12	0.13	0.95	0.28	2790	577	21.4	0.10	b.d.	b.d.	b.d.	b.d.	b.d.	b.d.	b.d.	b.d.	0.02	b.d.	0.03	b.d.	0.05	b.d.	86.8	54.1	1.0	0.10	0.07	10.0
9956d	35	Int.	14580	0.05	0.02	2.84	6.96	218	508	227.0	131.5	7.3	42.9	8.4	43.8	12.9	1.5	8.2	0.9	3.9	0.5	0.9	0.1	0.3	b.d.	22.6	15.9	9.8	0.5	9.0	12.7
9956d	36	Int.	15940	0.14	0.11	2.49	1.61	39	536	26.4	8.68	3.00	3.00	0.27	0.93	0.13	0.06	0.22	0.02	0.31	0.09	0.32	0.07	0.23	0.04	2.5	19.0	0.9	2.52	0.92	1.5
9956d	42	Prsm	15470	0.03	0.02	0.82	0.20	819	2015	123.7	2.19	0.49	1.11	0.11	0.36	0.03	b.d.	0.03	b.d.	0.02	b.d.	b.d.	b.d.	0.03	b.d.	37.3	117.9	15.7	0.03	0.66	26.9
9956d	43	Prsm	15540	0.03	b.d.	0.97	0.08	5170	1275	33.2	0.03	b.d.	b.d.	b.d.	b.d.	b.d.	b.d.	b.d.	b.d.	b.d.	b.d.	b.d.	b.d.	0.03	b.d.	117.3	17.3	7.7	0.17	0.05	50.3
9956d	44	Prsm	15950	b.d.	b.d.	0.89	0.54	2280	998	126.0	6.08	1.35	2.71	0.27	1.14	0.24	b.d.	0.06	0.02	0.14	0.03	0.06	b.d.	0.07	b.d.	75.7	23.9	67.0	0.07	1.68	135.0

Notes: The major elements (SiO_2, CaO) were analysed as controls of the rutile analyses especially to avoid analysing mixtures of rutile, titanite, epodite and calcite.

[a]Habit: Int. = interstitial; Prsm. = prismatic; [b]b.d. = below detection limit

TABLE 3: Analytical details of dated spots in rutile

Sample	Spot	Grain no.	Habit	Approx. concentrations (ppm)			Counts				Final isotope ratios							Age (Ma)			Data for inverse isochron				
				U	Th	U/Th	^{204}Pb cps	2σ int	^{206}Pb/^{204}Pb cps	%Pb*	^{207}Pb/^{235}U	2σ	^{206}Pb/^{238}U	2σ	err. corr.	^{207}Pb/^{206}Pb	2σ	^{206}Pb/^{238}U	2σ	% concordency	^{238}U/^{206}Pb	2σ	^{207}Pb/^{206}Pb	2σ	err. corr.
28a - 18	A	A	I	15.29	0.107	143	0	13	1741	99.68	0.422	0.041	0.056	0.002	0.05	0.0551	0.0055	350	14	100.9	17.92	0.71	0.055	0.006	0.26
56b - 2	C	C	I	27.79	<0.002	-	-17	16	3187	99.16	0.456	0.038	0.056	0.002	0.10	0.0595	0.0053	350	13	93.6	17.92	0.67	0.060	0.005	0.36
56b - 10	D	D	P	24.81	0.032	775	2	20	1384	99.53	0.415	0.045	0.054	0.002	0.12	0.0576	0.0072	337	13	97.7	18.66	0.77	0.058	0.007	0.45
28a - 18	E	D	P	25.13	0.004	6444	-11	17	3066	99.98	0.413	0.034	0.056	0.002	0.12	0.0541	0.0049	354	11	103.1	17.73	0.60	0.054	0.005	0.33
56b - 20	F	C	I	5.522	<0.002	-	2	16	319	99.30	0.456	0.080	0.056	0.003	0.05	0.0600	0.0100	348	20	100.9	17.99	1.10	0.060	0.010	0.20
56c - 3	G	E	I	19.74	1.730	11	3	14	765	99.61	0.438	0.038	0.057	0.002	0.13	0.0562	0.0054	359	12	99.8	17.45	0.61	0.056	0.005	0.42
56c - 9	H	F	I	27.14	3.990	7	-10	16	3250	99.50	0.427	0.034	0.055	0.002	0.10	0.0565	0.0046	347	12	96.9	18.08	0.65	0.057	0.005	0.26
56c - 13	I	G	P	7.58	<0.002	-	20	12	43	98.90	0.440	0.072	0.054	0.003	0.00	0.0620	0.0110	336	17	98.8	18.62	0.97	0.062	0.011	0.18
56c - 17	J	G	P	5.438	<0.002	-	-4	14	630	98.20	0.445	0.081	0.054	0.003	0.13	0.0670	0.0130	340	19	99.1	18.42	1.05	0.067	0.013	0.31
56c - 20	K	G	P	31.06	<0.002	-	-1	14	3381	99.99	0.385	0.028	0.053	0.002	0.09	0.0528	0.0039	335	11	103.2	18.73	0.63	0.053	0.004	0.26
56c - 21	L	G	P	42.12	0.254	166	11	13	431	99.86	0.392	0.023	0.054	0.002	0.08	0.0532	0.0034	338	11	101.9	18.55	0.62	0.053	0.003	0.19
56c - 24	M	G	P	38.51	<0.002	-	7	15	602	99.45	0.415	0.032	0.053	0.002	0.09	0.0571	0.0045	334	10	96.3	18.80	0.60	0.057	0.005	0.23
56d - 1	N	H	P	45.31	<0.002	-	5	15	1035	99.63	0.402	0.022	0.054	0.002	0.04	0.0548	0.0032	339	10	99.6	18.55	0.55	0.055	0.003	0.06
56d - 2	O	H	P	67.17	0.002	39512	6	16	1275	99.69	0.401	0.022	0.053	0.002	0.02	0.0553	0.0029	331	9	97.5	18.95	0.54	0.055	0.003	0.04
56d - 4	P	H	P	52.16	<0.002	-	-9	13	5850	100.15	0.387	0.023	0.055	0.002	0.03	0.0515	0.0032	344	10	104.5	18.25	0.53	0.052	0.003	0.26
56c - 22				5.44	<0.002	-	-5	19	584	99.50	0.380	0.100	0.052	0.004	0.16	0.0570	0.0150	326	26	112.0	19.23	1.59	0.057	0.015	0.24
28a - 11				1.407	0.030	48	9	13	18	94.60	0.380	0.180	0.054	0.006	0.06	0.0870	0.0450	335	38	223.3	18.55	2.13	0.087	0.045	0.61
28a - 35				3.69	4.350	1	-2	13	438	99.60	0.400	0.120	0.053	0.005	0.35	0.0550	0.0180	329	32	117.1	19.05	1.89	0.055	0.018	-0.60
56c - 9				43.2	0.619	70	1	14	4590	99.54	0.397	0.026	0.052	0.002	0.17	0.0553	0.0036	328	10	97.8	19.17	0.59	0.055	0.004	0.19
28a - 38				9.97	0.980	10	11	14	104	99.04	0.453	0.052	0.054	0.002	0.12	0.0599	0.0066	339	15	93.6	18.52	0.82	0.060	0.007	0.25
28a - 21				63.1	63.000	1	8	14	945	99.04	0.444	0.024	0.055	0.002	0.14	0.0597	0.0032	343	10	92.6	18.32	0.57	0.060	0.003	0.29
56b - 3				5.475	<0.002	-	-6	15	630	97.80	0.488	0.080	0.056	0.003	0.07	0.0700	0.0130	350	20	93.8	17.89	1.06	0.070	0.013	0.47
56b - 12				6.26	<0.002	-	-2	14	756	97.90	0.528	0.081	0.058	0.003	0.04	0.0700	0.0110	361	18	91.4	17.33	0.90	0.070	0.011	0.23
56b - 5				5.348	0.002	2674	-10	18	625	97.90	0.540	0.100	0.057	0.003	0.06	0.0700	0.0130	356	21	88.3	17.61	1.05	0.070	0.013	0.23
56b - 19				27.54	1.510	18	17	13	205	98.67	0.516	0.037	0.058	0.002	0.11	0.0636	0.0044	365	13	88.0	17.15	0.62	0.064	0.004	0.34
56b - 9				5.797	0.319	18	22	14	31	97.70	0.508	0.082	0.054	0.003	0.05	0.0720	0.0120	337	17	84.7	18.59	1.00	0.072	0.012	0.16
56b - 8				44.12	0.146	302	4	27	1273	97.90	0.522	0.064	0.055	0.003	0.13	0.0696	0.0086	345	15	82.5	18.18	0.83	0.070	0.009	0.19
56b - 17				47.95	0.002	26639	8	15	821	97.87	0.535	0.030	0.056	0.002	0.03	0.0702	0.0040	348	10	80.3	18.02	0.55	0.070	0.004	0.29
56c - 18				5.386	<0.002	-	-16	16	595	98.80	0.448	0.081	0.054	0.003	0.13	0.0630	0.0120	340	20	100.0	18.45	1.12	0.063	0.012	0.15
56c - 25				7.93	<0.002	-	-1	16	931	98.70	0.464	0.075	0.056	0.003	0.18	0.0600	0.0110	351	20	98.3	17.86	1.05	0.060	0.011	0.32
56c - 26				7.32	<0.002	-	15	14	62	98.80	0.469	0.077	0.058	0.003	0.16	0.0640	0.0110	364	20	97.8	17.18	0.97	0.064	0.011	0.41
56c - 23				7.93	<0.002	-	15	14	58	99.10	0.451	0.060	0.055	0.003	0.27	0.0602	0.0079	343	17	96.3	18.28	0.94	0.060	0.008	-0.01
56c - 31				6.88	0.395	17	12	15	64	98.50	0.464	0.076	0.054	0.003	0.12	0.0630	0.0110	336	18	94.9	18.69	1.01	0.063	0.011	0.35
56c - 14				10.04	<0.002	-	10	14	114	98.80	0.448	0.059	0.053	0.003	0.07	0.0622	0.0083	335	16	94.4	18.73	0.91	0.062	0.008	0.21
56c - 16				5.615	<0.002	-	-9	13	658	97.30	0.521	0.087	0.056	0.003	0.02	0.0740	0.0140	349	19	90.2	17.92	1.03	0.074	0.014	-0.03
56c - 12				53.45	<0.002	-	-2	19	6170	98.43	0.486	0.038	0.054	0.002	0.10	0.0656	0.0054	341	11	85.4	18.42	0.64	0.066	0.005	0.35
56c - 15				8.48	0.038	221	-7	13	918	97.40	0.490	0.062	0.052	0.003	0.09	0.0730	0.0100	325	16	83.8	19.31	0.97	0.073	0.010	0.34
28a - 13				13.66	1.017	13	8	14	194	98.69	0.475	0.055	0.056	0.002	0.01	0.0628	0.0073	350	14	92.1	17.89	0.74	0.063	0.007	0.19
28b - 8				8.86	0.157	56	8	15	123	98.90	0.439	0.064	0.055	0.003	0.68	0.0608	0.0095	346	17	99.4	18.12	0.92	0.061	0.010	-0.22
28b - 10				106.1	4.580	23	12	12	969	99.56	0.410	0.018	0.053	0.002	0.05	0.0558	0.0024	336	9	96.7	18.71	0.52	0.056	0.002	0.32

Notes : Sample: number is preceded by 99. Spots are labelled in Fig. 8. Grain no. is shown in Supplementary Figure S1. Habit: I = interstitial, P = prismatic. %Pb* = percentage radiometric Pb calculated by the methods of Andersen (2002). cps= integrated counts per second.

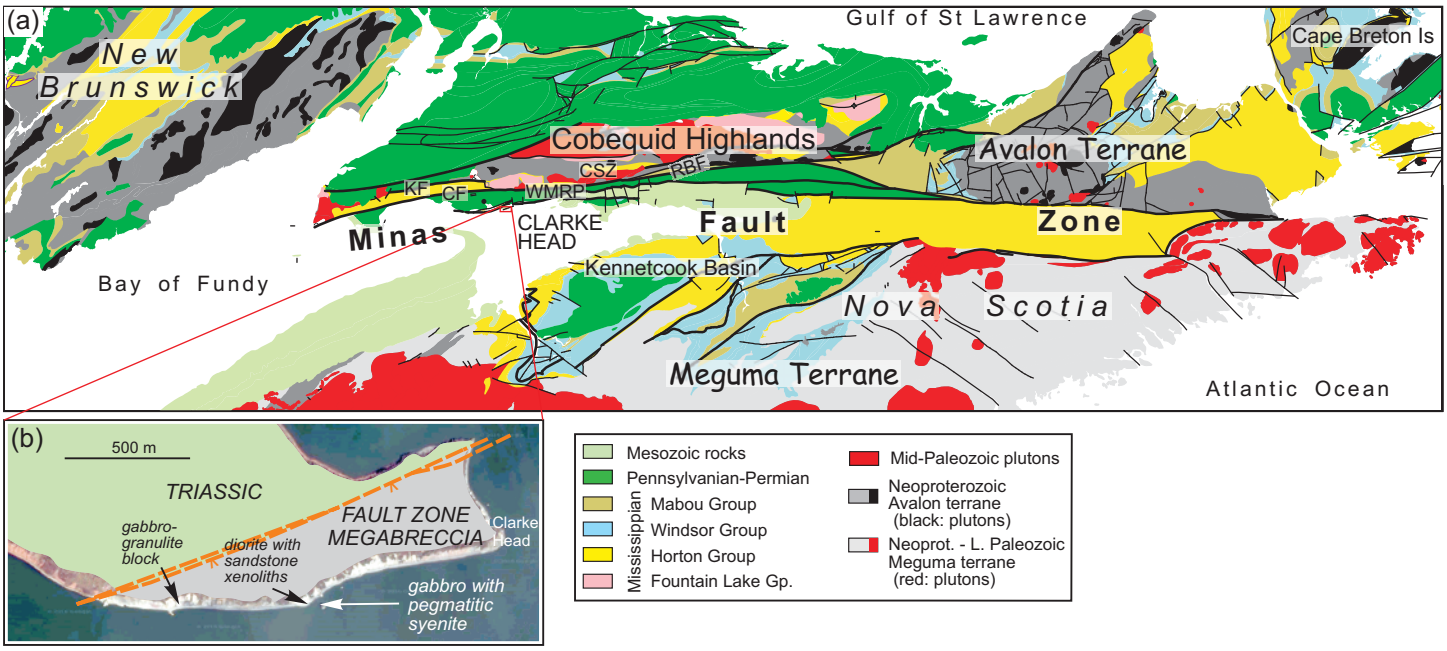
(a)
New Brunswick
Gulf of St Lawrence
Cape Breton Is
Cobequid Highlands
CSZ
RBF
KF
CF
WMRP
Avalon Terrane
Minas
CLARKE HEAD
Fault
Zone
Kennetcook Basin
Bay of Fundy
Nova Scotia
Meguma Terrane
Atlantic Ocean
(b)
500 m
TRIASSIC
FAULT ZONE MEGABRECCIA
Clarke Head
gabbro-granulite block
diorite with sandstone xenoliths
gabbro with pegmatitic syenite
Mesozoic rocks
Pennsylvanian-Permian
Mississippian
Mabou Group
Windsor Group
Horton Group
Fountain Lake Gp.
Mid-Paleozoic plutons
Neoproterozoic Avalon terrane (black: plutons)
Neoprot. - L. Paleozoic Meguma terrane (red: plutons)

Figure 1 R1

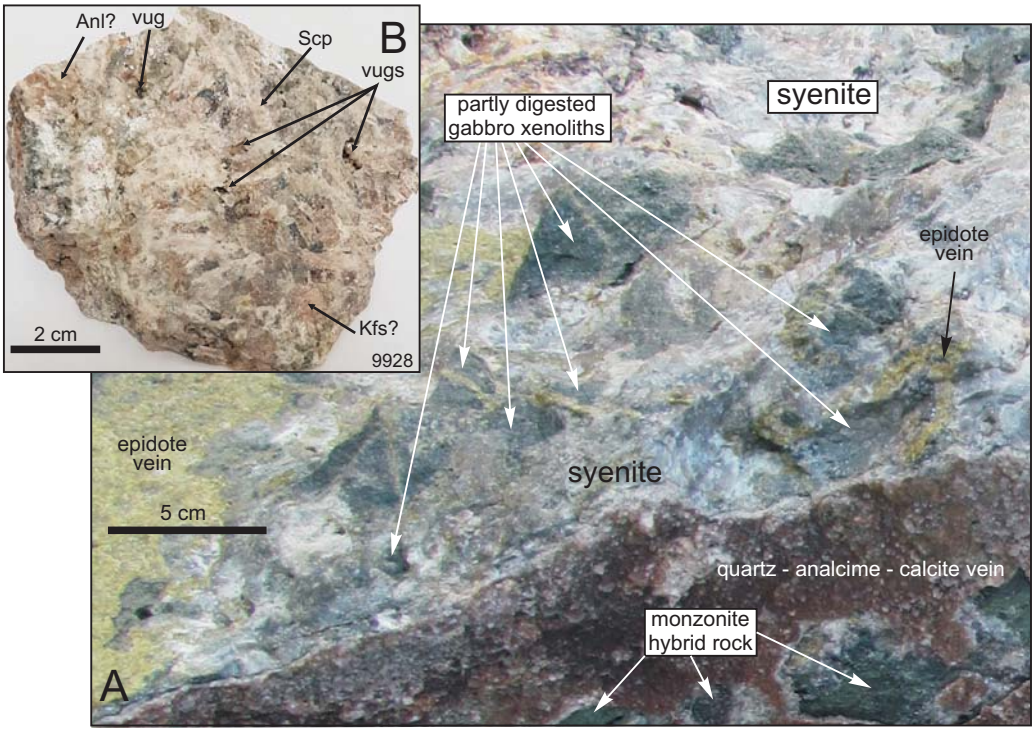
Anl?
vug
Scp
B
vugs
2 cm
Kfs?
9928
partly digested
gabbro xenoliths
syenite
epidote
vein
epidote
vein
5 cm
syenite
quartz - analcime - calcite vein
monzonite
hybrid rock
A

Figure 2 R1

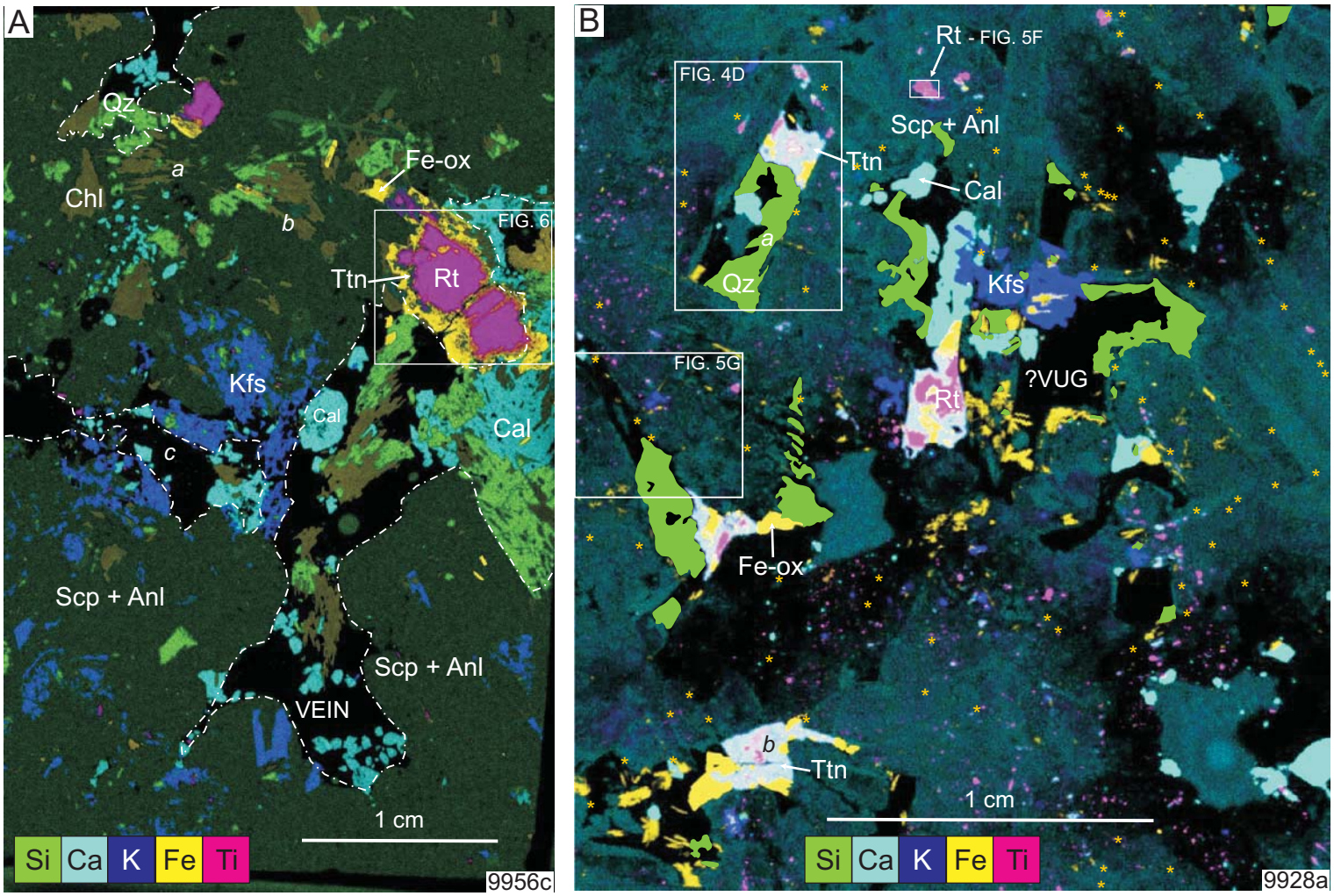
A
Qz
a
Chl
Fe-ox
b
FIG. 6
Ttn
Rt
Kfs
Cal
Cal
c
Scp + Anl
Scp + Anl
VEIN
1 cm
Si Ca K Fe Ti
9956c
B
Rt - FIG. 5F
FIG. 4D
Scp + Anl
Ttn
Cal
a
Qz
Kfs
FIG. 5G
?VUG
Rt
Fe-ox
b
Ttn
1 cm
Si Ca K Fe Ti
9928a

Figure 3 R1

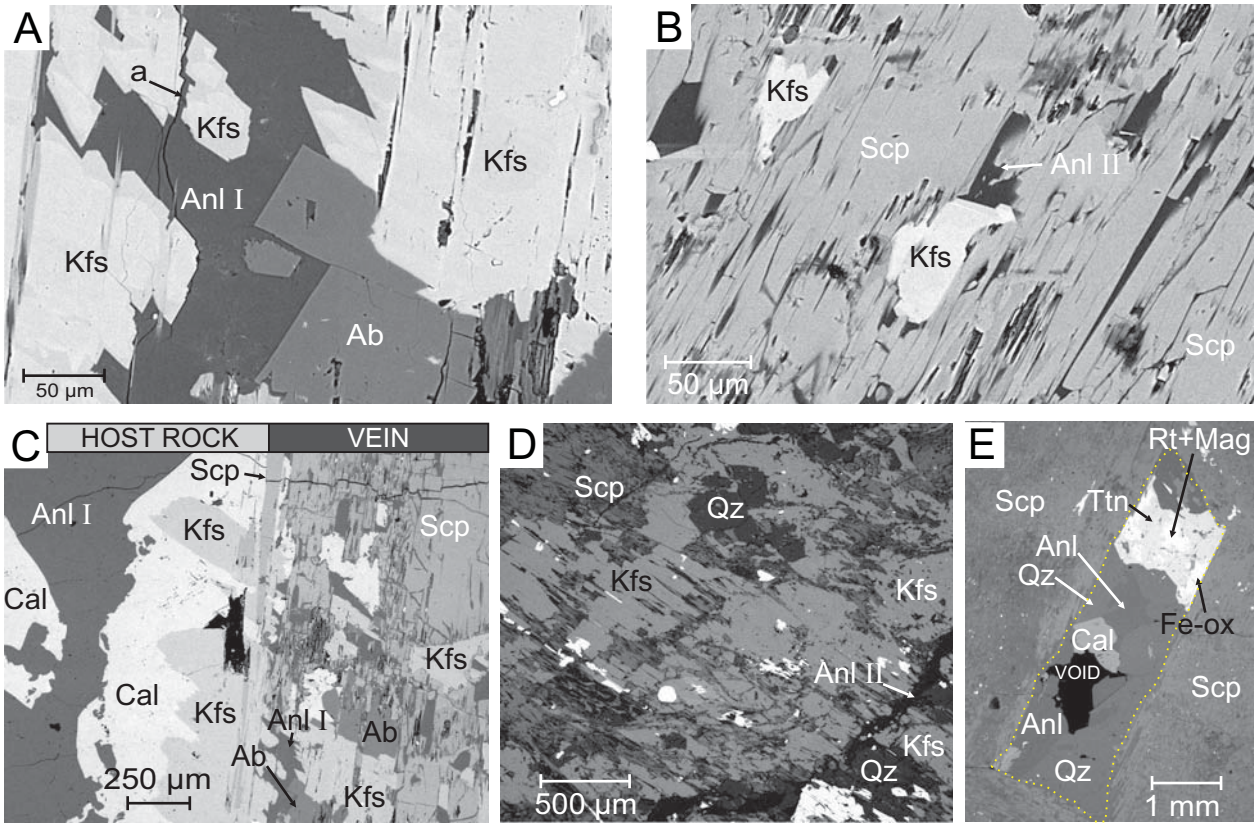
A
a
Kfs
Kfs
Anl I
Kfs
Ab
50 µm
B
Kfs
Scp
Anl II
Kfs
Scp
50 µm
C
HOST ROCK
VEIN
Scp
Anl I
Kfs
Scp
Cal
Kfs
Cal
Kfs
Anl I
Ab
Ab
250 µm
Kfs
D
Scp
Qz
Kfs
Kfs
Anl II
Kfs
Qz
500 µm
E
Rt+Mag
Scp
Ttn
Anl
Qz
Fe-ox
Cal
VOID
Scp
Anl
Qz
1 mm

Figure 4 R1

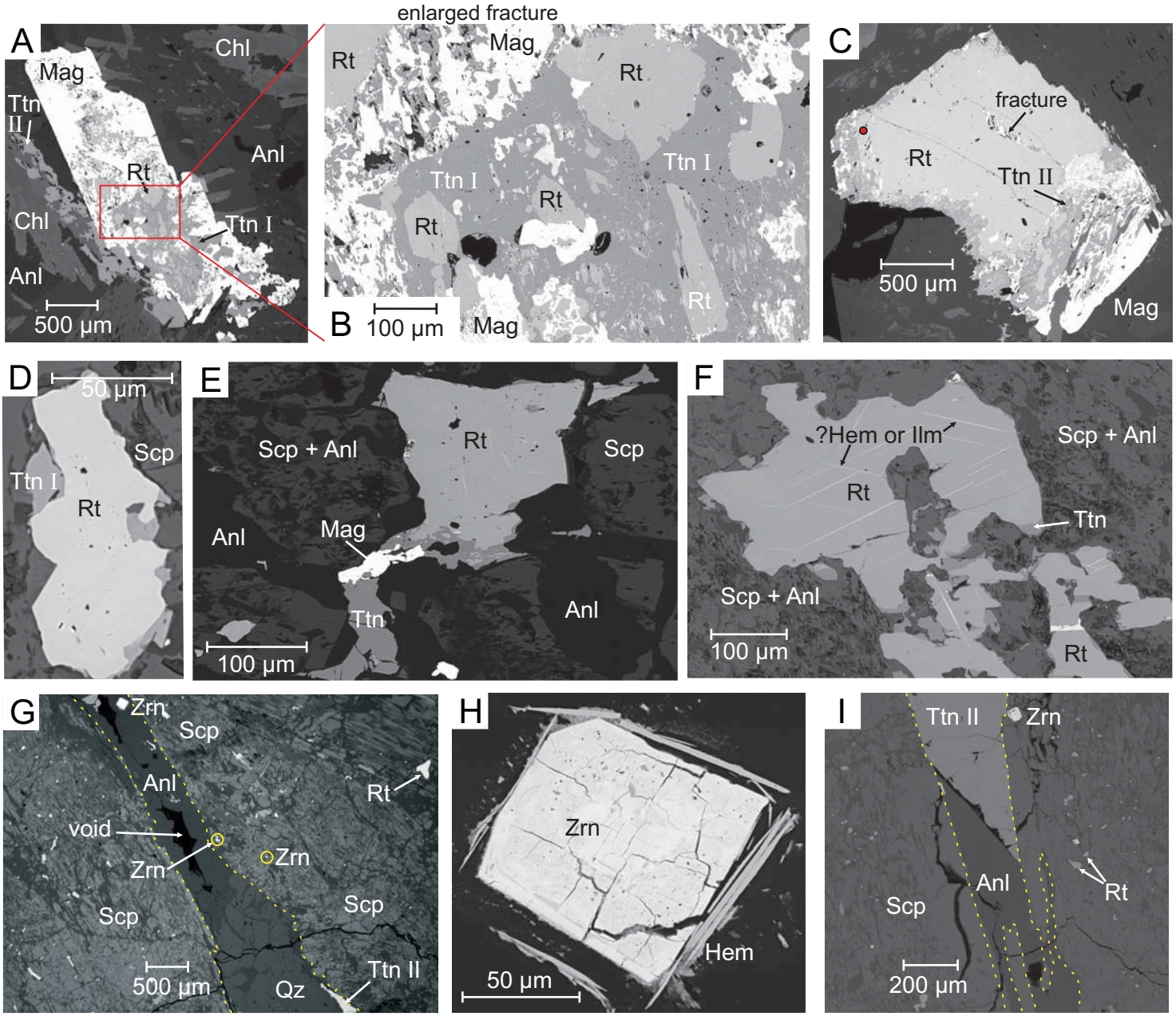
A
Chl
Mag
Ttn II
Anl
Rt
Chl
Ttn I
Anl
500 µm
enlarged fracture
Rt
Mag
Rt
Ttn I
Ttn I
Rt
Rt
Rt
B
100 µm
Mag
C
fracture
Rt
Ttn II
500 µm
Mag
D
50 µm
Scp
Ttn I
Rt
E
Scp + Anl
Rt
Scp
Anl
Mag
Ttn
Anl
100 µm
F
?Hem or Ilm
Scp + Anl
Rt
Ttn
Scp + Anl
100 µm
Rt
G
Zrn
Scp
Anl
Rt
void
Zrn
Zrn
Scp
Scp
500 µm
Qz
Ttn II
H
Zrn
Hem
50 µm
I
Ttn II
Zrn
Anl
Rt
Scp
200 µm

Figure 5 R1

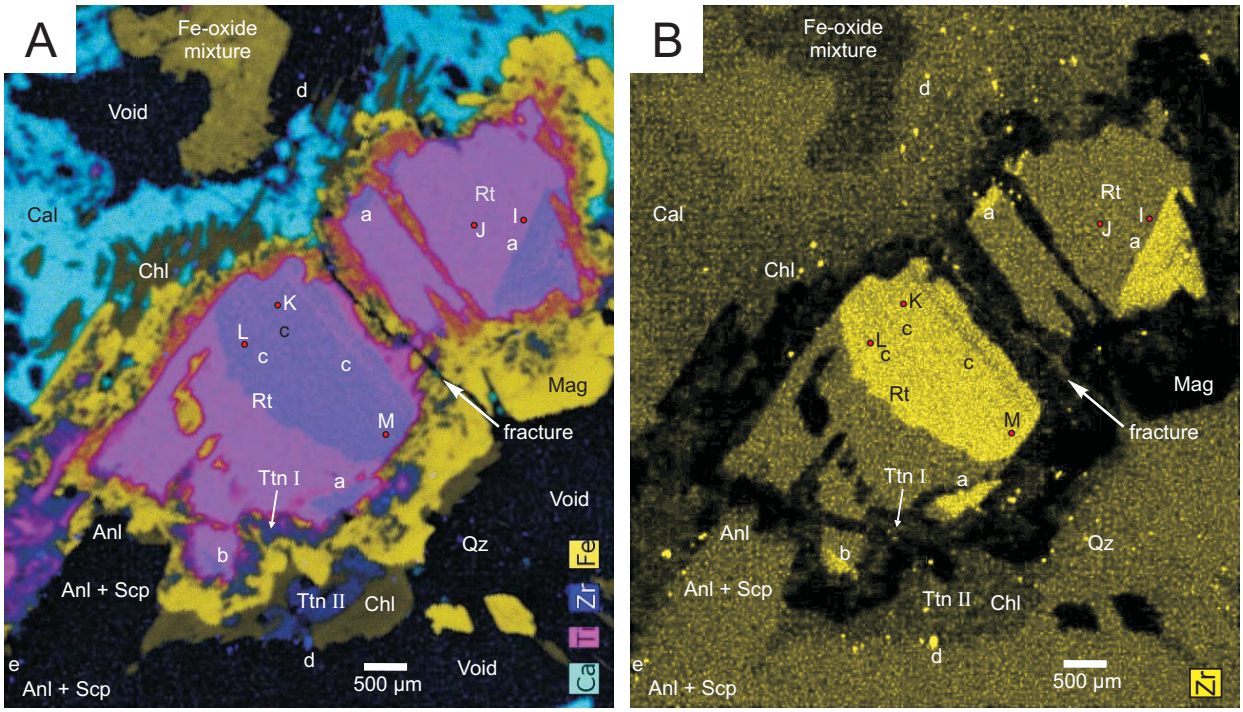
A
Fe-oxide mixture
Void
d
Cal
Chl
Rt
a
J
I
K
L
c
Mag
fracture
M
Ttn I
Void
Anl
b
Qz
Anl + Scp
Ttn II
Chl
e
500 µm
Fe
Zr
Ti
Ca
B
Fe-oxide mixture
d
Cal
a
Rt
J
I
Chl
K
L
c
Mag
Rt
fracture
M
Ttn I
Anl
b
Qz
Anl + Scp
Ttn II
Chl
e
500 µm
Ti

Figure 6 R1

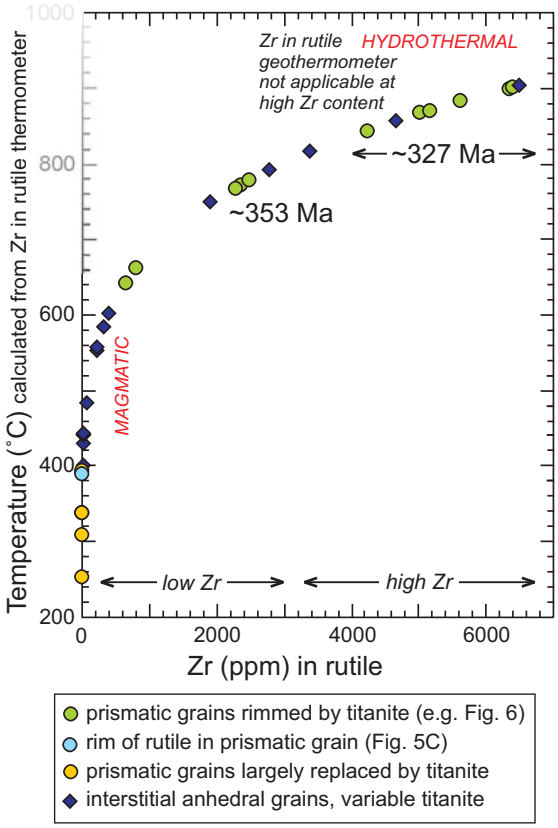
Zr in rutile geothermometer not applicable at high Zr content
HYDROTHERMAL
~327 Ma
~353 Ma
MAGMATIC
low Zr
high Zr
Temperature (˚C) calculated from Zr in rutile thermometer
Zr (ppm) in rutile
1000
800
600
400
200
0
2000
4000
6000
prismatic grains rimmed by titanite (e.g. Fig. 6)
rim of rutile in prismatic grain (Fig. 5C)
prismatic grains largely replaced by titanite
interstitial anhedral grains, variable titanite

Figure 7 R1

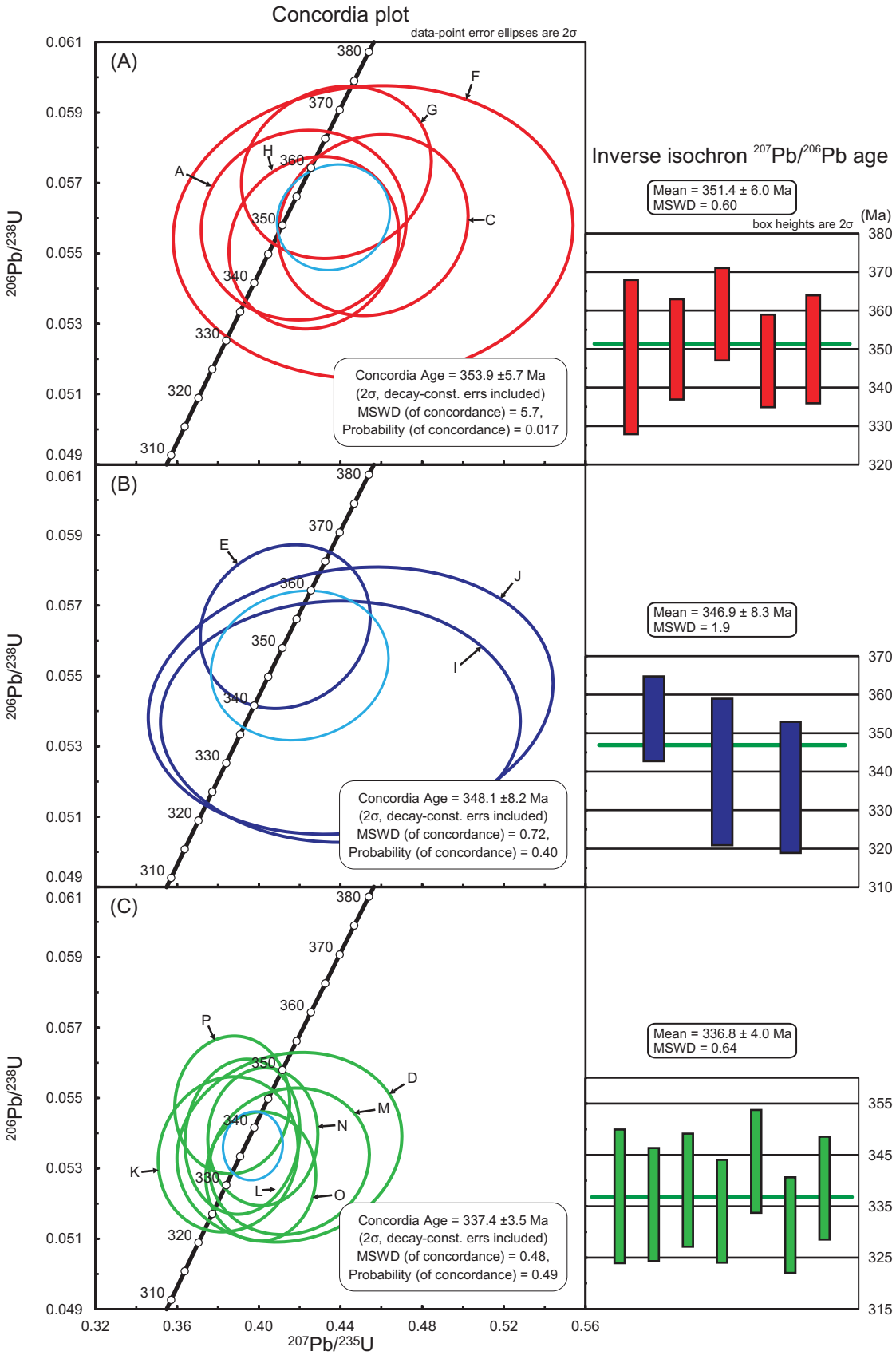
Concordia plot
data-point error ellipses are 2σ
(A)
(B)
(C)
Concordia Age = 353.9 ±5.7 Ma
(2σ, decay-const. errs included)
MSWD (of concordance) = 5.7,
Probability (of concordance) = 0.017
Concordia Age = 348.1 ±8.2 Ma
(2σ, decay-const. errs included)
MSWD (of concordance) = 0.72,
Probability (of concordance) = 0.40
Concordia Age = 337.4 ±3.5 Ma
(2σ, decay-const. errs included)
MSWD (of concordance) = 0.48,
Probability (of concordance) = 0.49
206Pb/238U
207Pb/235U
Inverse isochron 207Pb/206Pb age
box heights are 2σ
(Ma)
Mean = 351.4 ± 6.0 Ma
MSWD = 0.60
Mean = 346.9 ± 8.3 Ma
MSWD = 1.9
Mean = 336.8 ± 4.0 Ma
MSWD = 0.64

Figure 8 R1

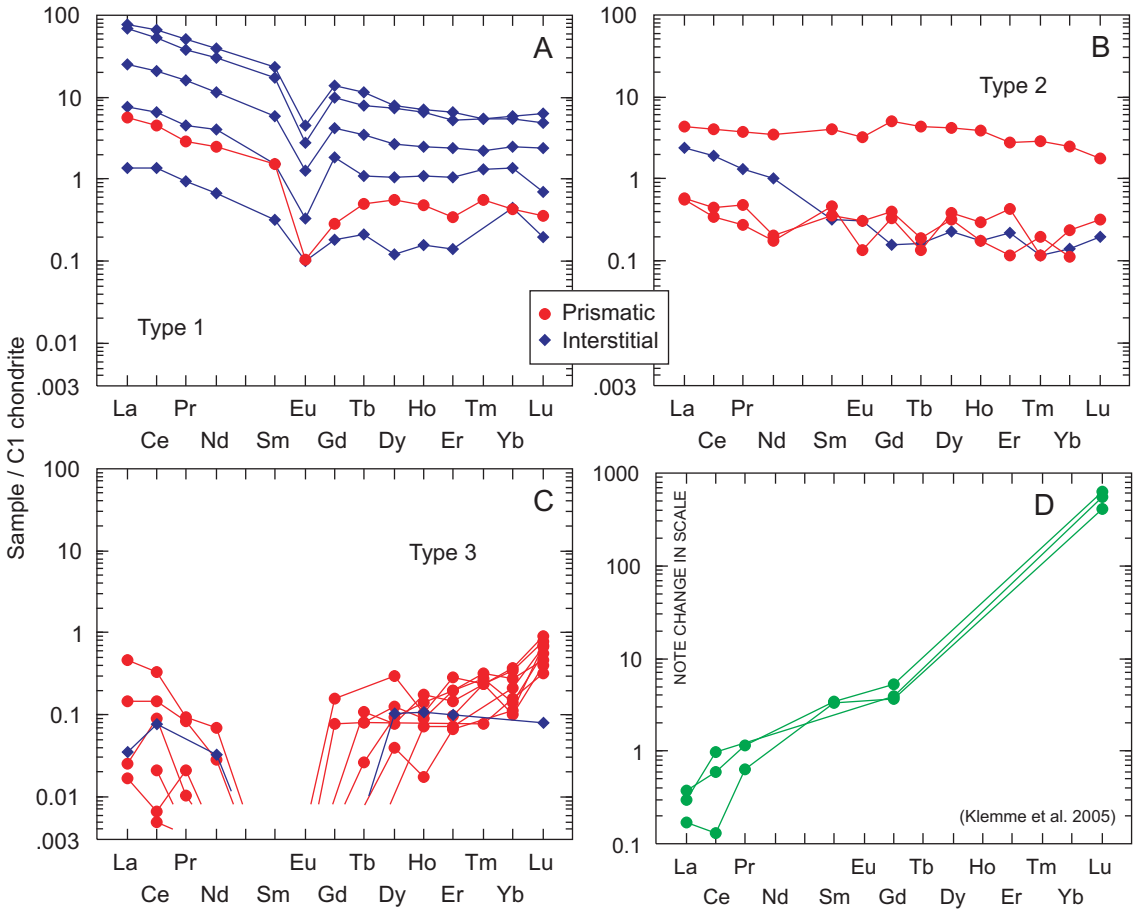
A
Type 1
B
Type 2
C
Type 3
D
NOTE CHANGE IN SCALE
(Klemme et al. 2005)
Prismatic
Interstitial
Sample / C1 chondrite
100
10
1
0.1
0.01
.003
1000
La Ce Pr Nd Eu Sm Tb Gd Ho Dy Tm Er Lu Yb

Figure 9 R1

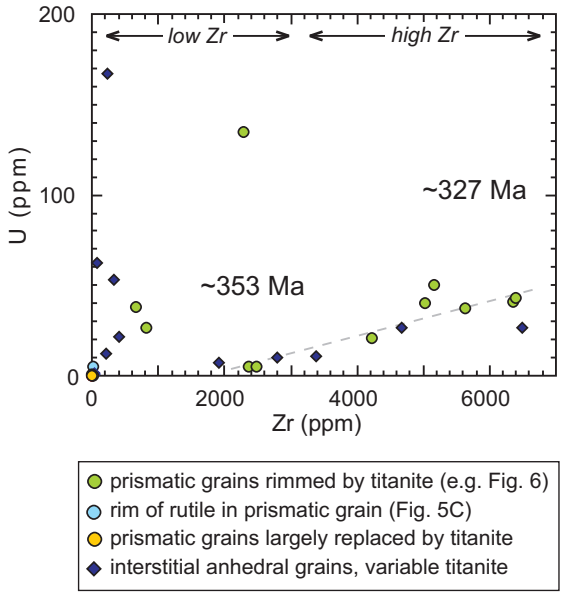
200
100
0
U (ppm)
low Zr
high Zr
~327 Ma
~353 Ma
0
2000
4000
6000
Zr (ppm)
prismatic grains rimmed by titanite (e.g. Fig. 6)
rim of rutile in prismatic grain (Fig. 5C)
prismatic grains largely replaced by titanite
interstitial anhedral grains, variable titanite

Figure 10 R1